Inorganic Chemistry

Article

pubs.acs.org/IC

Synthesis, Structure, and Magnetic Properties of $Dy_2Co_2L_{10}(bipy)_2$ and $Ln_2Ni_2L_{10}(bipy)_2$, *Ln* = La, Gd, Tb, Dy, and Ho: Slow Magnetic Relaxation in $Dy_2Co_2L_{10}(bipy)_2$ and $Dy_2Ni_2L_{10}(bipy)_2$

Fang-Hua Zhao,[†] Hui Li,[†] Yun-Xia Che,[†] Ji-Min Zheng,*[,†] Veacheslav Vieru,[‡] Liviu F. Chibotaru,*[,‡] Fernande Grandjean,[§] and Gary J. Long*[,§]

[†]Department of Chemistry, Nankai University, Tianjin 300071, China

[‡]Theory of Nanomaterials Group and INPAC—Institute of Nanoscale Physics and Chemistry, Katholieke Universiteit Leuven, Celestijnenlaan 200F, 3001 Heverlee, Belgium

[§]Department of Chemistry, Missouri University of Science and Technology, University of Missouri, Rolla, Missouri 65409-0010, United States

Supporting Information

ABSTRACT: The 3,5-dichlorobenzoate anion, L^-, serves as a bridging ligand and 2,2′-bipyridine, bipy, as a terminal bidentate ligand to yield, through hydrothermal syntheses, the tetranuclear clusters $Dy_2Co_2L_{10}(bipy)_2$, **1**, and $Ln_2Ni_2L_{10}(bipy)_2$, where *Ln* is the trivalent La, **2**, Gd, **3**, Tb, **4**, Dy, **5**, or Ho, **6**, ion. Single-crystal X-ray diffraction reveals that the six complexes are all isomorphous with the monoclinic $P2_1/c$ space group and with lattice parameters that decrease with the lanthanide contraction. The two cobalt(II) or nickel(II) and two *Ln*(III) cations are linked by the 10 L^- anions to generate Dy_2Co_2 or Ln_2Ni_2 3d−4f cationic heteronuclear clusters with a slightly bent Co···Dy···Dy···Co or Ni···*Ln*···*Ln*···Ni arrangement. Direct current magnetic susceptibility studies reveal that the complexes are essentially paramagnetic, with room-temperature $\chi_M T$ values close to the expected values for two cobalt(II) or nickel(II) and two *Ln*(III) cations. The temperature dependence of $\chi_M T$ for **1** and **5** is well reproduced by *ab initio* calculations with the inclusion of weak magnetic exchange between the cobalt(II) or nickel(II) and a dysprosium(III) and between two dysprosium(III) ions. The calculated magnetic exchange parameters are $J_{Dy-Co} = 0.2$ cm^{-1} and $J_{Dy-Dy} = 0.02$ cm^{-1} for **1** and $J_{Dy-Ni} = -0.2$ cm^{-1} and $J_{Dy-Dy} = 0.03$ cm^{-1} for **5**. Alternating current magnetic susceptibility studies reveal that **1** and **5** exhibit slow magnetic relaxation with effective energy barriers, U_{eff}, for the reversal of the magnetization for **1** of 82(2) cm^{-1} in a 0 Oe dc bias field and 79.4(5) cm^{-1} in a 1000 Oe dc bias field and, for **5**, 73(1) cm^{-1} in a 0 dc bias field; the calculated energies of 66.1(1) and 61.0(1) cm^{-1} for the first excited spin−orbit state of dysprosium(III) in **1** and **5** agree rather well with these effective energy barriers. The entire Arrhenius plots of the logarithm of τ, the relaxation rate of the magnetization in **1** and **5**, have been fit with contributions from quantum tunneling, direct Raman scattering, and Orbach thermal processes. The observation of a low-temperature magnetization reversal mechanism in **5** but not in **1** may be understood through the calculated exchange energy spectrum in their ground state.

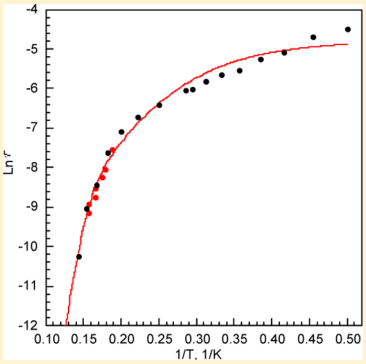

INTRODUCTION

Because of their potential applications in information storage, quantum computing, and spin-based molecular electronics,[1] single-molecule magnet complexes exhibiting slow magnetic relaxation are of special interest to physicists, chemists, and materials scientists. Many examples of single-molecule magnet complexes are polynuclear cation containing clusters in which the electronic spins of the cations are coupled by strong intramolecular exchange interactions to yield large effective magnetic moments, often with a predominant uniaxial anisotropy. These cation-containing clusters often combine 3d transition metal cations and 4f rare-earth cations, and numerous 3d−4f heteronuclear cationic clusters have been reported with magnetic properties that are significantly different from those of homonuclear cationic clusters. Although many of these clusters were copper(II)−rare-earth cationic clusters,[2] complexes containing other 3d metal ions, such as cobalt(II),[3] nickel(II),[4] and iron(II),[5] have been synthesized.

Rogez et al.[6] have suggested that to design 3d−4f heteronuclear cationic clusters with good single-molecule magnet behavior, nickel(II) is the best candidate among the 3d metal cations because it often exhibits a large single-ion zero-field splitting. Further, they note that, among the 4f rare-earth cations, terbium(III), dysprosium(III), and holmium(III), with the $^7F_6$, $^6H_{15/2}$, and $^5I_8$ ground-state electronic configurations, respectively, are the best 4f cations to use because of both their large ground-state *J*-values and their large magnetic anisotropies.[7] For the organic ligands used in the construction of the 3d−4f cationic clusters, several authors have

Received: June 12, 2014
Published: August 29, 2014

   dx.doi.org/10.1021/ic501374q | *Inorg. Chem.* 2014, 53, 9785−9799

Table 1. Crystal Data and Structural Refinement for 1−6

	$Dy_2Co_2L_{10}(bipy)_2$, **1**	$La_2Ni_2L_{10}(bipy)_2$, **2**	$Gd_2Ni_2L_{10}(bipy)_2$, **3**
formula	$Dy_2Co_2C_{90}H_{46}N_4O_{20}Cl_{20}$	$La_2Ni_2C_{90}H_{46}N_4O_{20}Cl_{20}$	$Gd_2Ni_2C_{90}H_{46}N_4O_{20}Cl_{20}$
fw, g/mol	2655.17	2607.685	2644.365
T, K	153(2)	153(2)	153(2)
cryst syst	monoclinic	monoclinic	monoclinic
space group	$P2_1/c$	$P2_1/c$	$P2_1/c$
a, Å	18.490(4)	18.626(4)	18.443(4)
b, Å	12.979(3)	13.001(3)	13.014(3)
c, Å	27.037(8)	27.197(8)	27.048(8)
α, deg	90	90	90
β, deg	130.742(19)	131.057(19)	130.853(19)
γ, deg	90	90	90
V, Å^3	4916(2)	4966(2)	4910(2)
Z	2	2	2
F(000)	2600	2568	2596
D (g/cm^3)	1.794	1.744	1.788
GOF	1.032	1.001	1.049
R_1, $wR_2[I > 2\sigma(I)]^a$	0.0295, 0.0575	0.0695, 0.1406	0.0356, 0.0724
	$Tb_2Ni_2L_{10}(bipy)_2$, **4**	$Dy_2Ni_2L_{10}(bipy)_2$, **5**	$Ho_2Ni_2L_{10}(bipy)_2$, **6**
formula	$Tb_2Ni_2C_{90}H_{46}N_4O_{20}Cl_{20}$	$Dy_2Ni_2C_{90}H_{46}N_4O_{20}Cl_{20}$	$Ho_2Ni_2C_{90}H_{46}N_4O_{20}Cl_{20}$
fw, g/mol	2647.713	2654.865	2659.725
T, K	153(2)	153(2)	153(2)
crystal syst	monoclinic	monoclinic	monoclinic
space group	$P2_1/c$	$P2_1/c$	$P2_1/c$
a, Å	18.432(4)	18.429(4)	18.404(4)
b, Å	13.017(3)	13.013(3)	13.004(3)
c, Å	27.049(8)	27.080(8)	27.060(8)
α, deg	90	90	90
β, deg	130.831(19)	130.946(19)	130.986(19)
γ, deg	90	90	90
V, Å^3	4910(2)	4905(2)	4889(2)
Z	2	2	2
F(000)	2600	2604	2608
D (g/cm^3)	1.791	1.797	1.807
GOF	1.007	1.031	1.079
R_1, $wR_2[I > 2\sigma(I)]^a$	0.0465, 0.0712	0.0447, 0.0720	0.0293, 0.0717

$^aR_1 = \sum(|F_o| - |F_c|)/\sum|F_o|$; $wR_2 = [\sum w(F_o^2 - F_c^2)^2/\sum w(F_o^2)^2]^{1/2}$.

suggested[8] the use of simple carboxylate anions, such as the formate, acetate, and benzoate anions, because they often serve as excellent bridging ligands that can facilitate the preparation of small polynuclear clusters. Finally, Schiff base ligands are often used as the terminal ligands that are needed to produce small polynuclear clusters.[9]

Herein the 3,5-dichlorobenzoate anion, L^-, has been used as a bridging ligand and 2,2′-bipyridine, bipy, has been used as a terminal ligand to prepare the small polynuclear clusters $Dy_2Co_2L_{10}(bipy)_2$, **1**, and $Ln_2Ni_2L_{10}(bipy)_2$, where *Ln* is the trivalent La, **2**, Gd, **3**, Tb, **4**, Dy, **5**, or Ho, **6**, ion. These clusters represent a new class of 3d−4f cationic heteronuclear clusters with a slightly bent Co···Dy···Dy···Co or Ni···*Ln*···*Ln*···Ni tetranuclear chain of cations. As will be shown below, of these six complexes only $Dy_2Co_2L_{10}(bipy)_2$, **1**, and $Dy_2Ni_2L_{10}(bipy)_2$, **5**, exhibit slow magnetic relaxation behavior with effective energy barriers, U_{eff}, for the reversal of the magnetization of 118(3) K or 82(2) cm^{-1} in a zero dc applied bias field and 114(1) K or 79.4(5) cm^{-1} in a 1000 Oe dc applied bias field for **1** and 104(1) K or 73(1) cm^{-1} for **5** in a zero dc applied bias field.

EXPERIMENTAL SECTION

The chemical reagents and solvents used were purchased commercially and used as received without further purification.

Synthesis of $Dy_2Co_2L_{10}(bipy)_2$, 1. A mixture of $Co(NO_3)_2{\cdot}6H_2O$ (0.087 g, 0.30 mmol), $Dy(NO_3)_3{\cdot}6H_2O$ (0.091 g, 0.20 mmol), 3,5-dichlorobenzoic acid (0.38 g, 2.0 mmol), and 2,2′-bipyridine (0.047 g, 0.32 mmol) was added to 6 mL of a 5 to 1 solution of water and ethanol. The pH was then adjusted to 5.0 with Na_2CO_3. The resulting mixture was sealed in a 25 mL Teflon-lined stainless steel vessel, heated at 140 °C for 3 days in an oven, and then slowly cooled to room temperature. Red block-shaped crystals of **1** were obtained with a 43% yield based on Dy. Anal. Calcd for $Dy_2Co_2C_{90}H_{46}N_4O_{20}Cl_{20}$: C 40.71, H 1.75, N 2.11. Found: C 40.80, H 1.70, N 2.19. IR (KBr): ν, cm^{-1}, 3073(m), 1606(vs), 1562(s), 1442(s), 1384(s), 1170(m), 1095(m), 870(m), 785(m), 759(m).

Synthesis of $La_2Ni_2L_{10}(bipy)_2$, 2. The reaction conditions are similar to those of the preparation of **1** described above except that $La(NO_3)_3{\cdot}6H_2O$ and $Ni(NO_3)_2{\cdot}6H_2O$ replaced $Dy(NO_3)_3{\cdot}6H_2O$ and $Co(NO_3)_2{\cdot}6H_2O$. Light blue-green block-shaped crystals of **2** were obtained with a 38% yield based on La. Anal. Calcd for $La_2Ni_2C_{90}H_{46}N_4O_{20}Cl_{20}$: C 41.45, H 1.78, N 2.15. Found: C 41.58, H 1.86, N 2.23. IR (KBr): ν, cm^{-1}, 3068(m), 1597(vs), 1560(s), 1444(s), 1396(s), 1156(m), 1093(m), 873(m), 785(m), 735(m).

Synthesis of $Gd_2Ni_2L_{10}(bipy)_2$, 3. The reaction conditions are similar to those of the preparation of **1** described above except that

dx.doi.org/10.1021/ic501374q | Inorg. Chem. 2014, 53, 9785−9799

$Gd(NO_3)_3·6H_2O$ and $Ni(NO_3)_2·6H_2O$ replaced $Dy(NO_3)_3·6H_2O$ and $Co(NO_3)_2·6H_2O$. Light blue-green block-shaped crystals of **3** were obtained with a 35% yield based on Gd. Anal. Calcd for $Gd_2Ni_2C_{90}H_{46}N_4O_{20}Cl_{20}$: C 40.88, H 1.75, N 2.12. Found: C 40.79, H 1.83, N 2.18. IR (KBr): ν, cm^{-1}, 3070(m), 1595(vs), 1560(s), 1442(s), 1398(s), 1153(m), 1090(m), 874(m), 785(m), 736(m).

Synthesis of $Tb_2Ni_2L_{10}(bipy)_2$, 4. The reaction conditions are similar to those of the preparation of **1** described above except that $Tb(NO_3)_3·6H_2O$ and $Ni(NO_3)_2·6H_2O$ replaced $Dy(NO_3)_3·6H_2O$ and $Co(NO_3)_2·6H_2O$. Light blue-green block-shaped crystals of **4** were obtained with a 40% yield based on Tb. Anal. Calcd for $Tb_2Ni_2C_{90}H_{46}N_4O_{20}Cl_{20}$: C 40.83, H 1.75, N 2.12. Found: C 40.84, H 1.71, N 2.10. IR (KBr): ν, cm^{-1}, 3072(m), 1581(vs), 1535(s), 1432(s), 1374(s), 1150(m), 1097(m), 861(m), 784(m), 722(m).

Synthesis of $Dy_2Ni_2L_{10}(bipy)_2$, 5. The reaction conditions are similar to those of the preparation of **1** described above except that $Ni(NO_3)_2·6H_2O$ replaced $Co(NO_3)_2·6H_2O$. Light blue-green block-shaped crystals of **5** were obtained with a 40% yield based on Dy. Anal. Calcd for $Dy_2Ni_2C_{90}H_{46}N_4O_{20}Cl_{20}$: C 40.72, H 1.75, N 2.11. Found: C 40.75, H 1.71, N 2.07. IR (KBr): ν, cm^{-1}, 3069(m), 1580(vs), 1530(s), 1432(s), 1374(s), 1150(m), 1090(m), 860(m), 780(m), 720(m).

Synthesis of $Ho_2Ni_2L_{10}(bipy)_2$, 6. The reaction conditions are similar to those of the preparation of **1** described above except that $Ho(NO_3)_3·6H_2O$ and $Ni(NO_3)_2·6H_2O$ replaced $Dy(NO_3)_3·6H_2O$ and $Co(NO_3)_2·6H_2O$. Light blue-green block-shaped crystals of **6** were obtained with a 47% yield based on Ho. Anal. Calcd for $Ho_2Ni_2C_{90}H_{46}N_4O_{20}Cl_{20}$: C 40.64, H 1.74, N 2.11. Found: C 40.69, H 1.70, N 2.02. IR (KBr): ν, cm^{-1}, 3069(m), 1533(s), 1442(s), 1374(s), 1150(m), 1090(m), 870(m), 785(m), 720(m).

Physical Methods. Elemental analyses have been performed by using a PerkinElmer model 240 CHN elemental analyzer. Infrared spectra were obtained between 4000 and 400 cm^{-1} in KBr pellets by using a Nicolet Magna-IR 560 infrared spectrometer.

X-ray Crystallographic Studies. Suitable single crystals of **1**–**6** were selected and mounted in air on thin glass fibers. Accurate unit cell parameters were determined by a least-squares adjustment of these parameters to agree with the 2θ scattering angles, and the intensity data were measured at 153(2) K by using a Rigaku R-axis Rapid IP area detector with 0.710 73 Å Mo Kα radiation. The intensities were corrected for Lorentz and polarization effects as well as for absorption by using an empirical multiscan technique. All structures were solved by direct methods and refined by full-matrix least-squares fitting on F^2 by using SHELX-97.[10] All non-hydrogen atoms and ions were refined with anisotropic thermal parameters. The positions of the hydrogen atoms were calculated theoretically. The crystallographic data and structural refinement parameters for **1**–**6** are summarized in Table 1, and selected bond distances are given in Tables S1 and S2.

Magnetic Studies. Magnetic studies were performed on samples of **1**–**6** anchored in Parafilm wax by using a Quantum Design MPMS superconducting quantum interference magnetometer. The magnetization has been measured from 0 to ±6 or ±8 T with a Quantum Design PPMS system.

The dc magnetic susceptibilities were measured between 300 and 2 or 1.8 K in a 0.01 and 0.10 T applied magnetic field; there were virtually no differences between the results obtained upon warming after zero-field cooling and upon subsequent cooling. The resulting molar magnetic susceptibilities, χ_M, have been corrected for the diamagnetic contribution of the sample holder and the wax used to anchor the samples. The resulting χ_M values were also corrected for the intrinsic diamagnetic susceptibilities of the compounds by using the values of −0.001 322 emu/mol for **1** and −0.001 324 emu/mol for **2**–**6** obtained from Pascal's constants.

The dc magnetizations have been measured at 2 K between ±6 for **5** and ±8 T for **1**–**6**. The magnetization of **5** was subsequently measured at seven different temperatures between 2 and 10 K in an applied magnetic field of 0 to 8 T. In these magnetization studies, the sweep rate of the applied field varied between 1 mT/s at the lower field and 6 mT/s at the higher field.

Subsequently, the ac molar magnetic susceptibilities of **1** and **4**–**6** have been measured in a ±3 Oe ac field and a zero dc bias field at several frequencies between 300 and 10 000 Hz during warming from 2 to 12 K for **1** and 2 to 17 K for **4**, between 20 and 1500 Hz during warming from 2 to 17 K for **5**, and between 2500 and 9500 Hz during warming from 2 to 15 K for **6**. The ac molar susceptibility of **1** was subsequently measured in a ±3 Oe ac field and a 1000 Oe dc bias field at several frequencies between 300 and 10 000 Hz during warming from 2 to 12 K.

RESULTS

Single-Crystal Structural Results. Single-crystal X-ray structural analysis reveals that **1**–**6** are isomorphous; hence the discussion will mostly concentrate on the crystal structure of $Dy_2Ni_2L_{10}(bipy)_2$, **5**. Complex **5** crystallizes in the monoclinic $P2_1/c$ space group with an asymmetric unit that consists of one independent nickel(II) cation, one independent dysprosium(III) cation, one 2,2′-bipyridine molecule, and five 3,5-dichlorobenzoate anions, L^-. As is shown in Figure 1, the nickel(II) cation is coordinated by four oxygens from two L^- anions and two 2,2′-bipyridine nitrogens, to yield a distorted NiO_4N_2 octahedral coordination environment; the dysprosium(III) cation has a monocapped triangular prismatic coordination environment (see Figure S1 in the Supporting Information) made up of seven oxygens from seven L^- anions, with O6#1, O8, and O9 in one trigonal plane and O7#1, O5, and O2 in the second trigonal plane; O4 is found at the capped site and forms a bridge between the nickel(II) and the dysprosium(III) ions. The Ni–O and Ni–N bond distances are all in the range of 2.009(3) to 2.451(3) Å, and the Dy–O bond distances are all in the range of 2.259(3) to 2.473(3) Å; all of these distances are normal.[4]

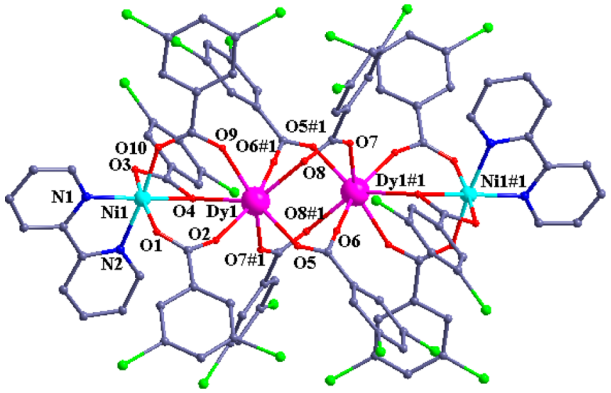

Figure 1. Structure of the $Dy_2Ni_2L_{10}(bipy)_2$, **5**, cluster showing the coordination environments of its nickel(II) and dysprosium(III) cations. The symmetry transformation for the #1 sites is $1 - x$, $2 - y$, $1 - z$.

The carboxylate moiety in the 3,5-dichlorobenzoate anions, L^-, adopts both bidentate and tridentate coordination modes in the structure of **1**–**6**; in two of the six L^- ligands O3 is bonded to Co1 or Ni1 and O4 serves as a bridging ligand between the Co1 or Ni1 and the *Ln*1 cations. Further, in **2**–**6** the Ni1–O4 bond distance is always the longest and decreases from 2.558(6) Å in **2** to 2.446(3) Å in **6**, and the *Ln*1–O4 bond distance is also always the longest and decreases from 2.559(6) Å in **2** to 2.451(2) Å in **6**; the Ni–O4–*Ln* bond angle increases from 101.90° in **2** to 104.67° in **6**. In comparison, in **1** the Co1–O4 bond distance is much larger at 2.718(2) Å, the Dy1–O4 is smaller at 2.424(2) Å, and the Co–O4–Dy bond angle is smallest at 101.03°. It should be noted in Table 1 that the refinement factors, R_1 and R_2, for **1** are the best reported for the

dx.doi.org/10.1021/ic501374q | Inorg. Chem. 2014, 53, 9785–9799

six compounds, and thus it seems that the substantially longer Co−O4 bond distance in **1** may be real. However, alternative refinements starting with a range of Co−O4 bond distances while keeping the Co−Dy distance constant reveal that reasonably acceptable refinements may be obtained with a 2.641(2) Å Co−O4 bond distance, a 2.491(2) Å Dy−O4 bond distance, a 101.45(8)° Co−O4−Dy bond angle, and a U_{iso} of 0.0485(7) Å^2; the corresponding R_1-factor has increased from 0.0295 to 0.0316, and the R_2-factor has increased from 0.0575 to 0.0658. Thus, it may be best to consider that the Co−O4 bond distance is in the range of 2.641(2) to 2.718(2) Å.

The two nickel(II) cations and two central dysprosium(III) cations in **5** are linked by ten 3,5-dichlorobenzoate anions, L^-, to generate the tetranuclear Dy_2Ni_2 cluster with a slightly bent Ni···Dy···Dy···Ni arrangement in which the nickel(II) and dysprosium(III) cations are linked by one tridentate and two bidentate carboxylate anions; the two central dysprosium(III) cations are linked by four bidentate carboxylate anions. In **5** the Ni···Dy and Dy···Dy distances are 3.887(2) and 4.049(4) Å, respectively, and the Ni−O4−Dy and Ni···Dy···Dy angles are 104.26(2)° and 153.95(4)°, respectively. In **1**−**6** the tetranuclear clusters are, as expected, all very similar. The bond metrics for the remaining compounds are given in Tables S1 and S2.

No intermolecular hydrogen bonds were observed in the structure of **5**; the closest intermolecular Ni···Ni and Ni···Dy distances are 7.528(2) and 10.637(3) Å, respectively.

Although a few *Ln*−Ni heteronuclear cationic complexes have been reported,[4,11] tetranuclear Ln_2Ni_2 clusters are relatively rare, and they have always displayed a cubane arrangement;[11d,e] the approximately linear but slightly bent Ni···Dy···Dy···Ni arrangement found in **5** is much more unusual.[11a,b] Because of the terminal 2,2′-bipyridine ligands and the bidentate bridging carboxylate ligands, the tetranuclear clusters in **1**−**6** do not enter into intermolecular bonding to form either one- or two-dimensional compounds.

In view of the differing magnetic properties of $Dy_2Co_2L_{10}(bipy)_2$, **1**, and $Dy_2Ni_2L_{10}(bipy)_2$, **5**, it was deemed of value to study in detail both the dependence of the crystal structures and the bonding upon the nature of the rare-earth ions, *Ln*(III), and any differences observed for cobalt(II) and nickel(II) in **1** and **5**, respectively. In the following discussion all the lattice parameters and distances have been obtained from crystals studied at 153 K. The role that the lanthanide contraction plays upon the crystal structure and bond distances in **1**−**6**, as well as the dependence of the Shannon and Prewitt effective ionic radii[12] upon the identity of the rare-earth ion, is shown in Figure S2 and is discussed in detail in the Supporting Information.

The dependence of the unit cell lattice parameters upon the nature of the *Ln*(III) ion in **1**−**6** is shown in Figure 2. From this figure it is immediately clear that the length of the *a*-axis of **3**−**6** decreases linearly with a slope of −0.012(3) Å/atomic number, a slope that is identical to that expected from the lanthanide contraction; see Figure S2. In contrast the length of the *b*-axis is close to constant and the *c*-axis is virtually constant for **3**−**6**.

The bond distances in **3**−**6** also reflect the importance of the lanthanide contraction. Specifically, the *Ln*−Ni distance in **3**−**6** decreases linearly from **3** to **6** with a slope of −0.0078(4) Å/atomic number. Further, as expected, the 3.9732(11) Å Dy−Co distance in **1** is 0.0863(2) Å longer than the 3.8869(13) Å Dy−Ni distance in **5**. In addition the *Ln*−O5 and *Ln*−O6 bond

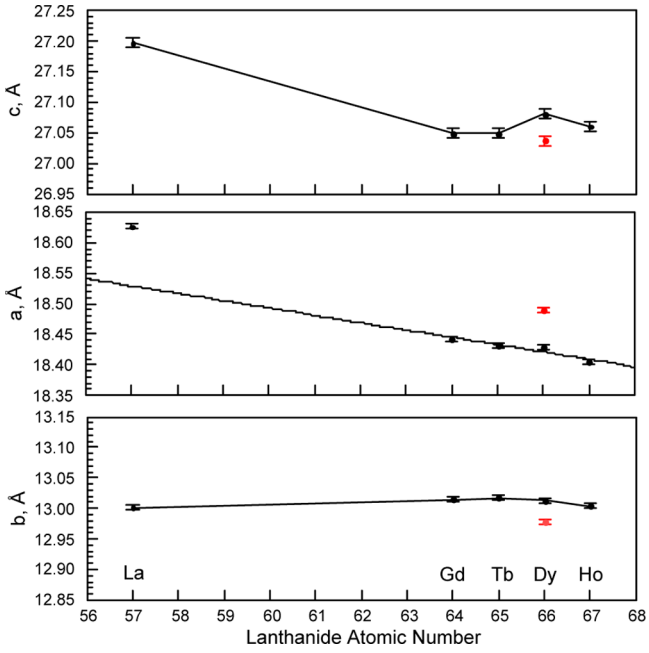

Figure 2. Dependence of the length of the unit cell axes on the *Ln*(III) atomic number. The data for the nickel(II) compounds, **2**−**6**, are shown in black, and those for the cobalt(II) compound, **1**, are shown in red. The *a*-axis for **3**−**6** decreases with a slope of −0.012(3) Å/atomic number, as shown by the fit.

distances are clearly related to the lanthanide contraction (see Figure 3), with slopes that are similar to the −0.0121(2) Å/

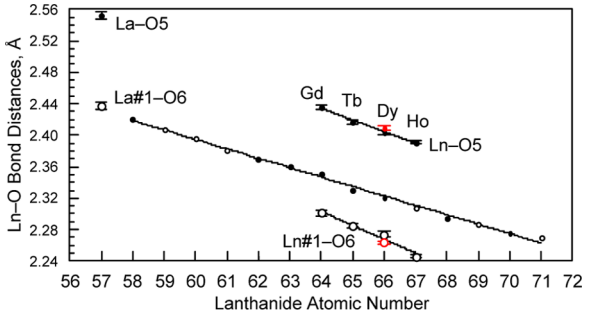

Figure 3. Dependence of the *Ln*−O bond lengths on the lanthanide contraction. The data for the nickel(II) compounds, **2**−**6**, are shown in black, those for the cobalt(II) compound, **1**, are shown in red, and the expected lanthanide contraction obtained from the *Ln*(III) effective ionic radii and a two-coordinate oxygen(−II) radius of 1.35 Å is shown in the center. The **3**−**6** *Ln*−O5 and *Ln*#1−O6 bond lengths decrease with slopes of −0.0145(9) and −0.018(2) Å/atomic number.

atomic number but with *Ln*−O5 bond lengths that are longer than would be expected and *Ln*−O6 bond lengths that are shorter than would be expected from the *Ln*(III) and oxygen(−II) effective ionic radii.

In conclusion it is apparent that for the nickel(II) **2**−**6** compounds the *a*-axis lattice parameters are highly correlated with the lanthanide contraction except for the *a*-axis in $La_2Ni_2L_{10}(bipy)_2$, **2**, which is larger than expected; the *b*- and *c*-axis parameters are not influenced by the lanthanide contraction but rather are close to constant. In **3**−**6** the *Ln*−O5, *Ln*−O6, *Ln*−O7, and *Ln*−O8 bond lengths all correlate nicely with the lanthanide contraction, but, again, the corresponding La−O bond lengths in **2** are longer than

dx.doi.org/10.1021/ic501374q | Inorg. Chem. 2014, 53, 9785−9799

Table 2. Modified Curie–Weiss Law Fits[a] of $\chi_M T$ of 1–6

compound	H, T	χ_0, emu/mol	C, emu K/mol	θ, deg	μ_{eff}, μ_B/mol	300 K $\chi_M T$, emu K/mol
$Dy_2Co_2L_{10}(bipy)_2$, **1**	0.01	0.0125(3)	30.67(7)	−4.38(9)	15.66(2)	33.78
	0.10	0.0049(3)	33.44(7)	−4.78(9)	16.35(2)	34.09
$La_2Ni_2L_{10}(bipy)_2$, **2**	0.01	0.007 84(5)	1.75(2)	9.2(9)	3.74(2)	4.18
	0.10	0.004 82(1)	2.404(3)	−0.58(5)	4.385(3)	3.85
$Gd_2Ni_2L_{10}(bipy)_2$, **3**	0.10	0.000 344(9)	17.580(2)	−0.016(5)	11.857(1)	17.68
$Tb_2Ni_2L_{10}(bipy)_2$, **4**	0.01	0.0046(2)	24.49(4)	−3.75(8)	13.99(1)	25.51
	0.10	0.0018(1)	26.18(4)	−3.89(7)	14.47(1)	26.37
$Dy_2Ni_2L_{10}(bipy)_2$, **5**	0.01	0.0270(2)	26.59(5)	−2.4(1)	14.58(1)	34.35
	0.10	0.0100(2)	30.22(6)	−3.9(1)	15.55(2)	32.58
$Ho_2Ni_2L_{10}(bipy)_2$, **6**	0.01	0.0336(3)	28.3(1)	−6.0(2)	15.04(3)	37.60
	0.10	0.0105(4)	33.05(4)	−9.4(2)	16.26(1)	35.00

[a]The fits are over the temperature range of 30 to 300 K for **1**–**4** and 40 to 300 K for **5** and **6**. The statistical errors are given in parentheses, and $\mu_{eff} = (3kC/N\beta^2)^{1/2} = 2.828C^{1/2} = 2.828[(\chi_M - \chi_0)(T - \theta)]^{1/2}$. The accuracy for the 300 K $\chi_M T$ is ca. ±0.02 emu K/mol.

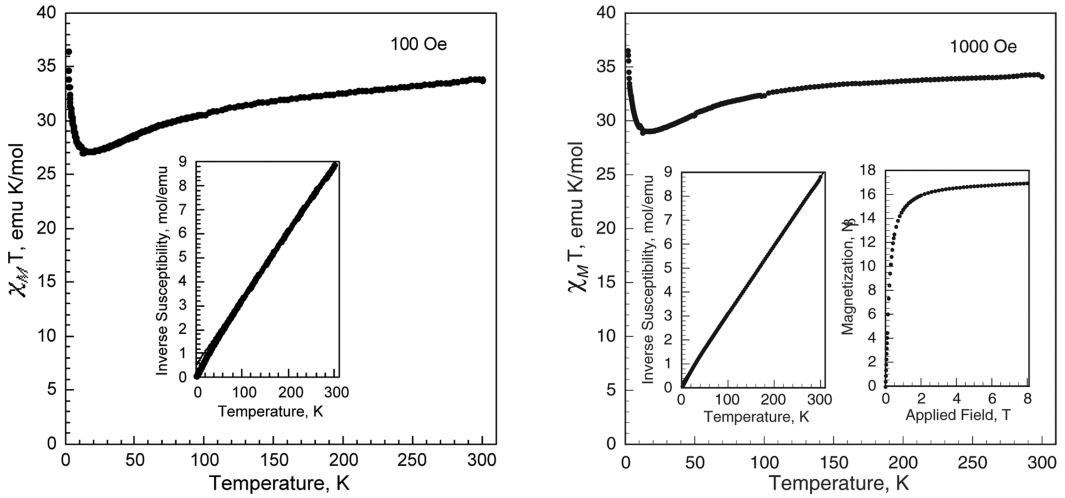

Figure 4. Temperature dependence of $\chi_M T$ obtained in a 100 Oe, left, and a 1000 Oe, right, applied dc magnetic field for $Dy_2Co_2L_{10}(bipy)_2$, **1**. Left inset: $1/\chi_M$ of **1** with a linear fit from 100 to 300 K. Right two insets: $1/\chi_M$ of **1** with a linear fit from 20 to 300 K and the 2 K magnetization of **1**. In both insets the fit of $1/\chi_M$ is mostly hidden by the data points.

expected based on the lanthanide contraction. The major difference between $Dy_2Co_2L_{10}(bipy)_2$, **1**, and $Dy_2Ni_2L_{10}(bipy)_2$, **5**, resides in their unit cell parameters. In cobalt(II)-containing **1** the *a*-axis is substantially longer than in nickel(II)-containing **5**. In addition, the monoclinic β-angle of 130.74(2)° in **1** is smaller than the angle of 130.95(2)° in **5**. Also in **1** and **5** there are at most small differences in the Dy–Co and Dy–Ni distances as well as in the bridging Dy–O bond lengths.

Magnetic Properties. Magnetic susceptibility measurements have been performed on crystalline samples of **1**–**6** in applied magnetic fields of 100 and 1000 Oe or 0.01 and 0.10 T between 1.8 or 2.0 and 300 K. At both applied fields $1/\chi_M$, which is virtually linear at higher temperatures, has been fit with the Curie–Weiss law over the temperature range given in Table S3. This table gives the resulting Curie constants, C, the Weiss temperatures, θ, and the corresponding effective magnetic moments, μ_{eff}. These results indicate that at these higher temperatures the compounds are all essentially paramagnetic. However, for paramagnetic compounds, the resulting $\chi_M T$ and corresponding μ_{eff} values are all higher and the Weiss temperatures, θ, are more negative than would be expected. This is an indication of the presence of a differing, but in several cases a substantial temperature-independent paramagnetic molar susceptibility, a presence that will also be apparent as a rather large positive slope in the temperature dependence of $\chi_M T$, as will be shown and discussed below.

As a consequence of the above observations, $\chi_M T$ has been fit with the modified Curie–Weiss law,

$$\chi_M T = \chi_0 T + \frac{CT}{T - \theta}$$

where χ_0 is a temperature-independent contribution to the molar magnetic susceptibility, i.e., predominately the second-order Zeeman contribution, $N\alpha$. The results of these fits are given in Table 2 and reveal, with the exception of $Gd_2Ni_2L_{10}(bipy)_2$, **3**, both that the χ_0 values are a factor of 10 to 100 times larger than that typically observed for many related complexes and that, as would be expected, the observed χ_0 values are always larger in a 100 Oe than in a 1000 Oe applied field. Indeed, relative to the χ_0 observed for $Gd_2Ni_2L_{10}(bipy)_2$, **3**, the remaining values obtained at 1000 Oe range from 5.2 times larger for $Tb_2Ni_2L_{10}(bipy)_2$, **5**, up to 30.5 times larger for $Ho_2Ni_2L_{10}(bipy)_2$, **6**. In addition, many of the resulting θ values are small and in the range of ca. ±9 K; most of these θ values are far smaller that those reported in Table S3. Over the temperatures range included in the fits (see Table 2), the χ_0 values include the $N\alpha$ contribution from the second-order Zeeman perturbation and may also model, in part, the contribution from small changes in the Stark level

dx.doi.org/10.1021/ic501374q | Inorg. Chem. 2014, 53, 9785–9799

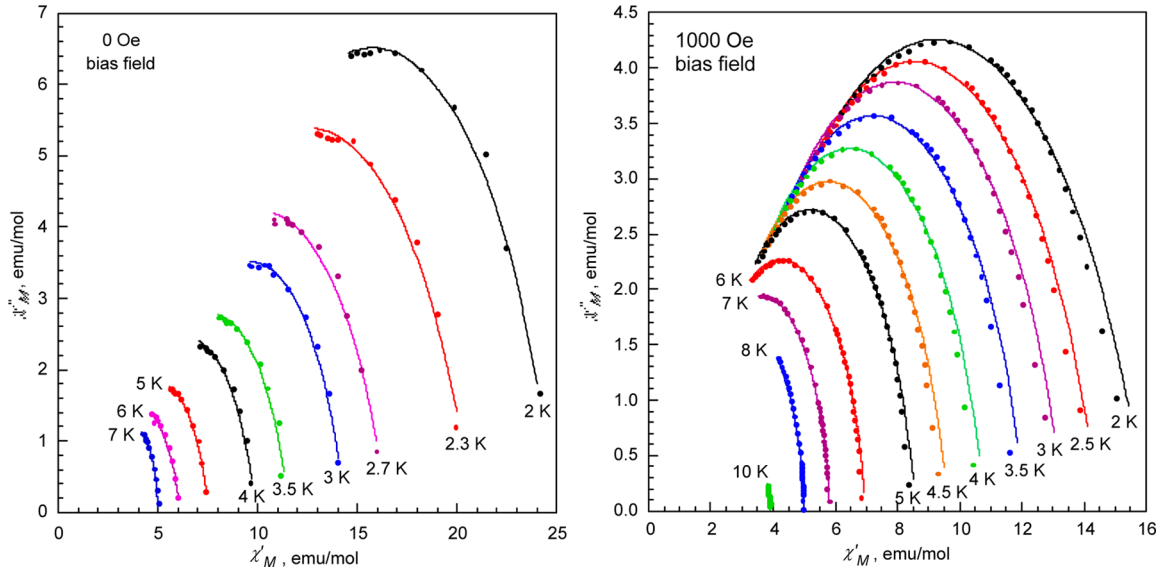

Figure 5. Cole−Cole plots obtained in a 0 Oe, left, and a 1000 Oe, right, applied dc bias field for $Dy_2Co_2L_{10}(bipy)_2$, **1**. The lines correspond to fits obtained with the generalized Debye model as given by equations S1 and S2 in the Supporting Information and the parameters given in the text.

populations, levels that are split by the weak crystal field at the lanthanide(III) ions.

At least at higher temperatures, to a good first approximation, the observed $\chi_M T$ obtained from the modified Curie−Weiss law fit and given in Table 2 for **1**−**6** should be the sum of the $\chi_M T$ of two *Ln*(III) ions and two cobalt(II) or nickel(II) ions if one assumes $S = 3/2$ for the cobalt(II) cations and $S = 1$ for the nickel(II) cations. In this approximation, in **2** each lanthanum(III) ion will have a diamagnetic $^1I_0$ electronic ground state and will make no contribution to the molar magnetic susceptibility of **2** in the absence of any second-order Zeeman contribution. In contrast, in **3** each gadolinium(III) ion will have an $^8S_{7/2}$ electronic ground state with $g = 2$ and will make a 7.877 emu K/mol contribution to the $\chi_M T$ of **3**, each terbium(III) ion will have a $^7F_6$ electronic ground state, for $J = 6$ with $g_J = 3/2$, and will make an 11.816 emu K/mol contribution to the $\chi_M T$ of **4**, each dysprosium(III) ion will have a $^6H_{15/2}$ electronic ground state, for $J = 15/2$ with $g_J = 4/3$, and will make a 14.171 emu K/mol contribution to the $\chi_M T$ of **1** and **5**, and each holmium(III) ion will have a $^5I_8$ electronic ground state, for $J = 8$ with $g_J = 5/4$, and will make a 14.067 emu K/mol contribution to the $\chi_M T$ of **6**. In all the compounds the *C* or $\chi_M T$ values found over the fitted temperature range (see Table 2) are in good to excellent agreement with the values obtained from the sum of the expected contributions given above.

Magnetic Properties of $Dy_2Co_2L_{10}(bipy)_2$, 1. The temperature dependence of $\chi_M T$ obtained for **1** between 2.0 and 300 K in an applied field of 100 and 1000 Oe is shown in Figure 4. At 100 Oe the $\chi_M T$ product decreases gradually with decreasing temperature from 33.78(2) emu K/mol at 300 K to a minimum of 27.14(2) emu K/mol at 17.6 K and then increases sharply to 36.40(2) emu K/mol at 2.0 K. The behavior is virtually the same at 1000 Oe except for the slightly larger $\chi_M T$ of 34.09(2) emu K/mol observed at 300 K. The slope in the linear portion of $\chi_M T$ above ca. 100 K is smaller at 1000 Oe than at 100 Oe, a difference that is indicative of the presence of a temperature-independent paramagnetic molar susceptibility in **1** as is shown in Table 2. As would be expected, the $1/\chi_M$ at both applied fields is essentially linear above 30 K; see the insets to Figure 4.

It is difficult to quantitatively fit the temperature dependence of $\chi_M T$ for **1**, but it appears that at least above 30 K the two dysprosium(III) and the two cobalt(II) ions do not undergo magnetic exchange coupling and that the increase in $\chi_M T$ above ca. 30 K is probably the result of a combination of the small but significant temperature-independent paramagnetic molar susceptibility, a change in the thermal population of the crystal-field split Stark levels of the two crystallographically equivalent dysprosium(III) ions, and, to a lesser extent, the presence of zero-field splitting of the ground state of the two crystallographically equivalent cobalt(II) ions. Indeed, the 300 K $\chi_M T$ values observed for **1** are indicative of the presence of two paramagnetic dysprosium(III) and two paramagnetic cobalt(II) ions if the latter ions have $S = 3/2$ and a *g*-factor of ca. 2.8, where the latter value is somewhat high because of the large χ_0 reported in Table 2.

The increase in $\chi_M T$ for **1** below 17.6 K is most likely an indication of the presence of some weak intramolecular ferromagnetic exchange between the two well-separated cobalt(II) ions as mediated by the two intervening dysprosium(III) ions. An *ab initio* calculation of the temperature dependence of $\chi_M T$ for **1** is presented below and supports the presence of weak ferromagnetic exchange both between dysprosium(III) and cobalt(II) and between dysprosium(III) and dysprosium(III).

The right most inset to Figure 4 indicates that the 2 K, 8 T magnetization of **1** is 16.93(3) Nβ and appears to be close to saturation. However, the expected saturation magnetization is given[13] by

$$M_{sat} = 2(g_{Dy(III)}J_{max} + g_{Co(II)}S_{Co(II)})$$
$$= 2\{(4/3)(15/2) + 2(3/2)]$$

or $M_{sat} = 26$ Nβ, which is substantially higher than the observed value as an apparent consequence of the large magnetic anisotropy associated with **1**. *Ab initio* calculations, presented below, show that the magnetization could saturate at or slightly below 18 Nβ. Further, the ±15 Oe coercivity observed at 2 K for **1** is experimentally no different from zero. Hence **1** exhibits no hysteresis at 2 K when the applied field sweep rate is as slow

dx.doi.org/10.1021/ic501374q | Inorg. Chem. 2014, 53, 9785−9799

as a few mT/s. Strictly speaking **1** cannot be considered to be a single-molecule magnet material, but, as shown below, ac magnetic studies do reveal slow relaxation of the magnetization. However, the 2 K quantum tunneling time of the magnetization of ca. 10^{-4} s is much shorter than the seconds to minutes of typical time required for a change in applied field during the recording of the magnetization shown in the inset. Hence, the magnetization relaxes many times during the change in field at and near a zero applied field, and, as a consequence, no remanence nor hysteresis is observed in the 2 K magnetization of **1**. The presence of quantum tunneling at 2 K is also confirmed by the *ab initio* calculations; see below.

The temperature dependence of the ac magnetization of **1** has been measured between 2 and 12 K in a 3 Oe oscillating field, in both a 0 and a 1000 Oe dc bias field, at several frequencies between 511 and 10 000 Hz. The temperature and frequency dependence of χ_M is shown in Figures S3 and S4, respectively. A Cole−Cole plot of χ_M'' vs χ_M' is shown in Figure 5. In this figure the solid lines correspond to fits with the generalized Debye model[14] by using the expressions given in the Supporting Information. In these fits, four parameters were fitted for each temperature, χ_∞, the adiabatic susceptibility extrapolated to infinite frequency, χ_0, the isothermal susceptibility extrapolated to zero frequency, τ, the magnetization relaxation time, and α, a parameter that quantifies the width of the τ distribution; if α = 0, the Cole−Cole plot will be a semicircle, and if α is greater than zero, the plot will become semioval shaped. For **1** all the α-values are between 0.1 and 0.2, values that are typical of this type of compound.

The temperature dependence of the logarithm of τ yields details on the magnetic relaxation pathways for the magnetization of **1**. A detailed analysis of the logarithm of τ in an Arrhenius plot was therefore undertaken. The corresponding fit of the Arrhenius plot for **1** from 2 to 10 K includes contributions from quantum tunneling, direct, Raman scattering, and Orbach thermal processes through the expression

$$\tau^{-1} = {\tau_{QTM}}^{-1} + AH^2T + CT^5 + {\tau_0}^{-1}\exp(-U_{eff}/k_BT) \quad (1)$$

where ${\tau_{QTM}}^{-1}$ corresponds to the relaxation frequency of the quantum tunneling relaxation process, A is the coefficient of the direct process, and C is the Raman scattering coefficient. The last term in this equation corresponds to a thermally activated Orbach process, where ${\tau_0}^{-1}$ is the attempt frequency and U_{eff} is the effective magnetization reversal barrier. In a zero applied dc field, the AH^2T term in eq 1 vanishes and the fit for a zero bias field shown in Figure 6 yields a quantum tunneling frequency, ${\tau_{QTM}}^{-1}$, of 6.9(5) × 10^4 s^{-1}, a Raman coefficient, C, of 1.9(6) s^{-1} K^{-5}, an attempt frequency, ${\tau_0}^{-1}$, of 54 × 10^9 s^{-1}, and an effective magnetization reversal barrier, U_{eff}, of 118(3) K or 82(2) cm^{-1}. In fitting the observed temperature dependence of the logarithm of τ, it was noticed that the attempt frequency, ${\tau_0}^{-1}$, was poorly defined and the frequency was kept constant to obtain the fit shown in Figure 6. This constant value is in the range usually observed for various slow relaxing clusters and molecules.[15] In the presence of the 1000 Oe bias field, the term AH^2T in eq 1 and the effect of the field on the quantum tunneling process should be taken into account. Unfortunately, in the absence of measurements at different applied bias fields, it was not possible to make a reasonable estimate of the A and B_2 coefficients in the field-dependent terms of the relaxation frequency, as given by eq 2,

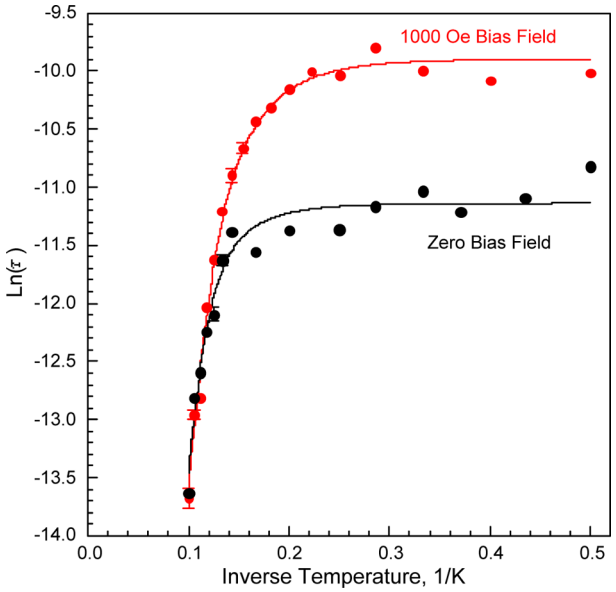

Figure 6. Arrhenius plot of the logarithm of the relaxation time of the magnetization of $Dy_2Co_2L_{10}(bipy)_2$, **1**, obtained in a 0 and 1000 Oe applied dc bias field. The lines correspond to fits with eq 1 and the parameters that are given in the text.

$$\tau^{-1} = AH^2T + \frac{B_1}{1 + B_2H^2} \quad (2)$$

Hence, A and B_2 were fixed to zero in the fit shown in Figure 6, a fit that yields a quantum tunneling frequency, ${\tau_{QTM}}^{-1}$, of 1.98(6) × 10^4 s^{-1}, a Raman coefficient, C, of 2.0(1) s^{-1} K^{-5}, an attempt frequency, ${\tau_0}^{-1}$, of 54 × 10^9 s^{-1}, and an effective magnetization reversal barrier, U_{eff}, of 114.2(7) K or 79.4(5) cm^{-1}. It is clear that the 1000 Oe applied bias field reduces the quantum tunneling frequency, i.e., the temperature-independent magnetization reversal frequency. The Raman coefficient, C, and the effective magnetization reversal barrier, U_{eff}, are not affected by the applied bias field. As is shown in Figure 6, below ca. 5 or 0.2 K^{-1}, the relaxation departs from that expected for a thermally activated process and becomes, at least in part, a quantum tunneling process[16,17] with a relaxation time that tends to reach a constant value.

The effective energy barrier for relaxation of the magnetization, U_{eff}, of 118(3) K or 82(2) cm^{-1} observed in the absence of a bias field for **1** matches the largest U_{eff} linear fit value reported at high temperature for another Dy_2Co_2 cobalt(II) complex.[18] However, it should be noted that the use of eq 1 to analyze the Arrhenius plot, rather than a linear fit, as is usually the case in many studies, is responsible for perhaps half of the larger U_{eff} observed in **1**. Indeed, if a linear fit of the Arrhenius plot between 7 and 10 K is used, a U_{eff} of 47(1) K or 33(1) cm^{-1} and 54(1) K or 38(1) cm^{-1} results in the 0 and 1000 Oe dc bias field.

Magnetic Properties of $La_2Ni_2L_{10}(bipy)_2$, 2. The magnetic properties of **2** (see Figure 7), which arise from the two paramagnetic nickel(II) ions at an intramolecular distance of 11.740(1) Å, are unusual because the χ_MT obtained in a 1000 Oe dc applied field is not constant but rather decreases linearly with decreasing temperature from 3.847(5) emu K/mol at 300 K to 2.562(5) emu K/mol at 40 K and then decreases more dramatically to 0.923(5) emu K/mol at 1.8 K. This type of behavior is indicative of the magnetic properties of a nickel(II) ion in the presence of zero-field splitting and an extensive

dx.doi.org/10.1021/ic501374q | Inorg. Chem. 2014, 53, 9785−9799

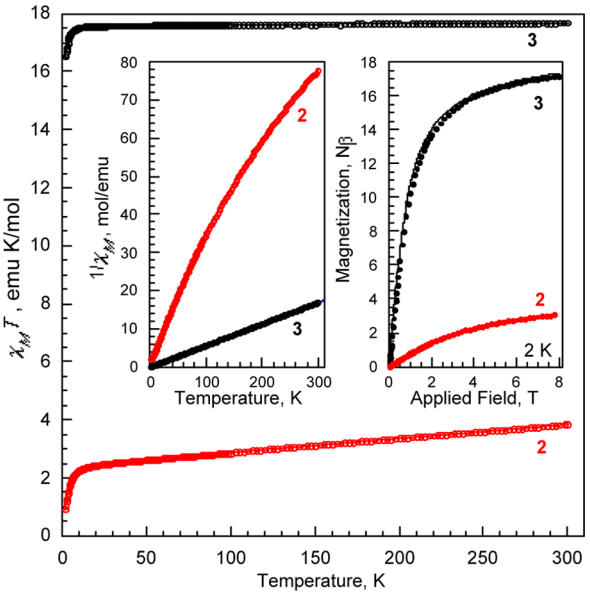

Figure 7. Temperature dependence of $\chi_M T$ obtained in a 1000 Oe applied dc field for $La_2Ni_2L_{10}(bipy)_2$, **2**, in red, and $Gd_2Ni_2L_{10}(bipy)_2$, **3**, in black, where both sets of $\chi_M T$ values include the fits discussed in the text, fits that are completely hidden by the data points. Left inset: $1/\chi_M$ of **2** and **3**. Right inset: the 2 K magnetization of **2** and **3**. For **3** the solid line is calculated with the fitted parameters for the susceptibility given in the text.

second-order Zeeman contribution, $N\alpha$, to its molar magnetic susceptibility. This is confirmed by an excellent fit of $\chi_M T$ from 1.8 to 300 K, which yields, for $S = 1$, a zero field splitting of $D = 7.05(2)$ cm^{-1}, with $g = 2.178(1)$, and $N\alpha = 0.00485(1)$ emu/mol. This essentially perfect fit is shown in Figure 7, and the components of this fit are shown in Figure S5A. A statistically slightly better, but visually identical, fit with $S = 1$, zero field splitting, and an axial g-tensor was obtained with $D = 6.34(6)$ cm^{-1}, $g_z = 2.38(2)$, $g_x = g_y = 2.083(8)$, and $N\alpha = 0.004\,85(1)$ emu/mol.

Because of the rather high value of $N\alpha$ in the above fits, the magnetic susceptibility of **2** was subsequently measured in a 100 Oe applied field in order to determine whether or not $N\alpha$ would increase as expected in a smaller applied field; a comparison of the 100 and 1000 Oe results is shown in Figure S6. This is indeed the case, as is confirmed by a fit of $\chi_M T$ for **2** obtained from 1.8 to 300 K in a 100 Oe applied field that yields an essentially perfect fit with a zero-field splitting of $D = 7.05(2)$ cm^{-1}, $g = 2.050(2)$, and $N\alpha = 0.006\,60(2)$ emu/mol; see Figure S7A. It should be noted that the $N\alpha$ value is similar to the χ_0 value reported in Table 2. At 100 Oe the fit obtained with an isotropic g-factor was statistically as valid as that obtained with an anisotropic g-factor.

Conventional wisdom indicates that for a zero-field splitting as small as ± 7 cm^{-1} the fits of $\chi_M T$ should be equally as good for either a positive or negative D-value. However, as is shown in Figures S5A–C, and S7A,B, this is clearly *not* the case for compound **2** in either a 100 or 1000 Oe applied field. From Figure S5C, it is clear that between 1.8 and 20 K the calculated $\chi_M T$ values are very different for a positive or a negative D-value and that a positive D of 7.05(2) cm^{-1} yields an excellent fit, whereas a negative D-value of -7.05 cm^{-1} yields a totally unacceptable fit.

Finally, as expected, a fit of the $\chi_M T$ observed for **2** with an isotropic Heisenberg exchange coupling Hamiltonian completely fails at both 100 and 1000 Oe applied fields. This failure may result from the long intramolecular distance between the two nickel(II) ions and contrasts with the successful fit[4b] of the temperature dependence of $\chi_M T$ observed for $[L_2Ni_2La][ClO_4]$, in which the two nickel(II) ions are close enough to lead to an intramolecular antiferromagnetic exchange interaction. However, as noted above, the shortest Ni(II)···Ni(II) intermolecular distance in **2** is 7.514(2) Å, and the possibility of a combination of zero-field splitting and a weak intermolecular antiferromagnetic exchange coupling contribution to the decrease in $\chi_M T$ below ca. 15 K is possible.

The 2 K magnetization of **2** is clearly not saturated in an 8 T applied magnetic field, but the observed value of 3.06(3) Nβ is

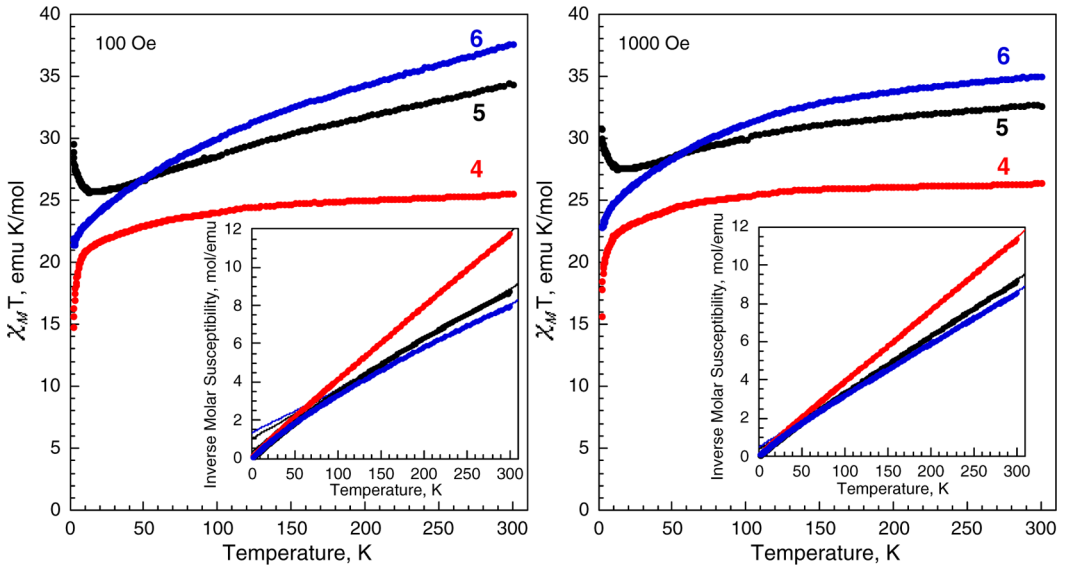

Figure 8. Temperature dependence of $\chi_M T$ for **4**–**6** obtained upon warming, after zero-field cooling, in an applied field of 100 Oe or 0.01 T, left, and 1000 Oe or 0.10 T, right. Insets: The temperature dependence of $1/\chi_M$ and its fit over the temperature ranges given in Table 2 with the Curie–Weiss law, fits that in some cases are mostly hidden by the data points.

dx.doi.org/10.1021/ic501374q | Inorg. Chem. 2014, 53, 9785–9799

consistent with the four unpaired electrons per mole expected in **2**. It should be noted that the 2 K magnetization of **2** is lower at all applied fields than twice that expected for a Brillouin curve for $S = 1$. This may be an indication that at 2 K there is some weak intermolecular antiferromagnetic exchange coupling that leads to an increasing canting of the antiferromagnetic moments with increasing applied field, a canting that is not fully complete even at 8 T.

Magnetic Properties of $Gd_2Ni_2L_{10}(bipy)_2$, 3. The magnetic properties of **3** indicate that it is fully paramagnetic and its $\chi_M T$ obtained in a 1000 Oe dc applied field arises from the sum of two paramagnetic gadolinium(III) and two paramagnetic nickel(II) ions. The observed $\chi_M T$ of **3** is 17.68(2) emu K/mol at 300 K and is essentially constant upon cooling to 17.54(2) emu K/mol at 12 K and then decreases slightly to 16.52(2) emu K/mol at 1.8 K. An essentially perfect fit of $\chi_M T$ for **3** between 1.8 and 300 K is obtained with two paramagnetic gadolinium(III) ions with $S = 7/2$ and $g = 2$ and two nickel(II) ions with $S = 1$ that exhibit zero-field splitting with $D = 5.81(3)$ cm^{-1}, $g = 1.912(7)$, and $N\alpha = 0.000\,334$ emu/mol; see Figures 7 and S8.

The 2 K magnetization of **3** is not quite saturated by an 8 T applied field, but the observed value of 17.17(3) Nβ is consistent with the 18 unpaired electrons per mole expected in **3** and the expected $M_{sat} = 2(g_{Gd(III)}J_{max} + g_{Ni(II)}S_{Ni(II)}) = 2[2(7/2) + 2(1)] = 18$ Nβ. The solid line in the right inset in Figure 7 is the magnetization curve calculated with the program[19] PHI for two paramagnetic gadolinium(III) ions with $S = 7/2$ and $g = 2$ and two nickel(II) ions with the parameters obtained from the fit of $\chi_M T$. The good agreement between the experimental 2 K magnetization and the solid line indicates that the two gadolinium(III) and two nickel(II) ions are completely independent, and there is no intramolecular exchange interaction in **3**. This behavior again contrasts with the intramolecular ferromagnetic interactions observed[4b] in $[L_2Ni_2Gd][ClO_4]$.

Magnetic Properties of $Tb_2Ni_2L_{10}(bipy)_2$, 4. The temperature dependence of $\chi_M T$ for **4** obtained between 1.8 and 300 K in a 100 and 1000 Oe applied field is shown in red in Figure 8. At 100 Oe $\chi_M T$ decreases with decreasing temperature from 25.51(2) emu K/mol at 300 K to 21.06(2) emu K/mol at 12 K and then decreases more rapidly to 14.81(2) emu K/mol at 1.8 K. The behavior is virtually the same at 1000 Oe with $\chi_M T$ decreasing from 26.37(2) emu K/mol at 300 K to 21.00(2) emu K/mol at 12 K and then more rapidly to 15.65(2) emu K/mol at 1.8 K. As a consequence of this smaller $\chi_M T$ at 300 K the slope in the linear portion of $\chi_M T$ above ca. 100 K is smaller at 1000 Oe than at 100 Oe, a difference that is indicative of the presence of a temperature-independent paramagnetic molar susceptibility in **4**, as shown in Table 2. As would be expected the $1/\chi_M$ at both applied fields is essentially linear above 30 K; see the insets in Figure 8.

It is difficult to quantitatively fit the temperature dependence of $\chi_M T$ for **4**, but it appears that at least above 30 K the two terbium(III) and the two nickel(II) ions do not undergo magnetic exchange coupling for the same reasons as mentioned above for **1**. The 300 K $\chi_M T$ values observed for **4** are also indicative of the presence of two paramagnetic terbium(III) and two paramagnetic nickel(II) ions if the latter ions have $S = 1$ and a g-factor of ca. 2.

Below ca. 12 K the more rapid decrease in $\chi_M T$ for **4** may result from a combination of zero-field splitting of the nickel(II), very weak intramolecular antiferromagnetic exchange between the terbium(III) and/or nickel(II) ions, and weak intermolecular antiferromagnetic exchange.

The magnetization of **4** obtained at 2 K and ±8 T (see Figure 9) is essentially saturated at 8 T at 20.17(3) Nβ, a value

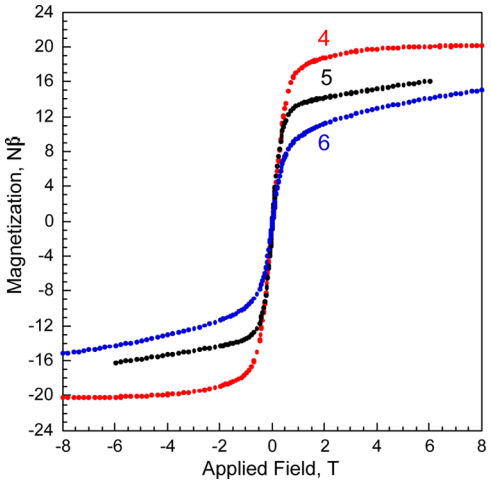

Figure 9. Magnetization at 2 K of $Tb_2Ni_2L_{10}(bipy)_2$, **4**, red, $Dy_2Ni_2L_{10}(bipy)_2$, **5**, black, and $Ho_2Ni_2L_{10}(bipy)_2$, **6**, blue.

that agrees well with the $M_{sat} = 22$ Nβ obtained for **4** with the expression given above $g_{Tb(III)} = 3/2$ and $J_{max} = 6$. No experimentally significant hysteresis is observed in the 2 K magnetization of **4**. Similar magnetization curves have been observed[4b] for some $LnNi_2$ clusters.

The temperature dependence of $\chi_M T$ shown in Figure 8 for **4** above ca. 50 K is rather similar to that exhibited[4b] by $[L'_2TbNi_2][ClO_4]$, where L'^{3-} is $\{(S)P[N(Me)N{=}CH\text{-}C_6H_3\text{-}2\text{-}O\text{-}3\text{-}OMe]_3\}^{3-}$. More specifically, the $\chi_M T$ of $[L'_2TbNi_2][ClO_4]$ first decreases very gradually and almost linearly from ca. 13 to 12 emu K/mol between 300 and 30 K, then increases slightly to ca. 13.5 emu K/mol at ca. 5 K, and finally decreases to ca. 12.3 emu K/mol at 2 K. The rather different behavior below 50 K may be attributed to the more separated nature of the Ni···Tb···Tb···Ni bridging arrangement in **4** as compared to the Ni···Tb···Ni bridging arrangement in $[L'_2TbNi_2][ClO_4]$.

No frequency dependence of the in-phase, χ_M', or out-of-phase, χ_M'', components of the ac susceptibility of **4** was observed between 2 and 17 K and 20 to 9500 Hz; see Figure S9.

Magnetic Properties of $Dy_2Ni_2L_{10}(bipy)_2$, 5. As might be expected, the temperature dependencies of $\chi_M T$ for $Dy_2Co_2L_{10}(bipy)_2$, **1**, and $Dy_2Ni_2L_{10}(bipy)_2$, **5**, are quite similar except for a small difference in their magnitudes. The temperature dependence of $\chi_M T$ for **5** obtained between 300 and 2 K in a 100 and 1000 Oe applied magnetic field is shown in black in Figure 8. At 100 Oe the $\chi_M T$ of **5** decreases almost linearly from 34.35(2) emu K/mol at 300 K to 25.60(2) emu K/mol at 12.6 K and then increases to 29.49(2) emu K/mol at 2 K. Qualitatively very similar results are obtained at 1000 Oe except that the $\chi_M T$ of 32.58(2) emu K/mol obtained at 300 K decreases to 27.43(2) emu K/mol at 12.6 K. The smaller 300 K $\chi_M T$ value obtained at 1000 Oe as compared to the value at 100 Oe indicates, as expected, a smaller value of the temperature-independent paramagnetic molar susceptibility of **5** in the larger applied field. Again, the 300 K $\chi_M T$ values observed for **5** are indicative of the presence of two paramagnetic dysprosium(III) and two paramagnetic nickel(II) ions if the latter ions have $S =$

dx.doi.org/10.1021/ic501374q | Inorg. Chem. 2014, 53, 9785−9799

1 and a *g*-factor of ca. 3.4, a factor that is large because of the large χ_0 reported in Table 2 at 100 Oe.

As was observed for **4** above, the $\chi_M T$ shown in Figure 8 for **5** has a rather different temperature dependence from that observed[4b] for $[L'_2DyNi_2][ClO_4]$, which exhibits an essentially constant $\chi_M T$ between 100 and 300 K. Below 100 K both compounds show a minimum in $\chi_M T$ at ca. 30 K for $[L'_2DyNi_2][ClO_4]$ and at 12.6 K for **5** followed by an increase at lower temperatures. Another distinct difference is that $[L'_2DyNi_2][ClO_4]$ exhibits a decrease in $\chi_M T$ below ca. 7 K, a decrease that is not observed in **5**.

The magnetization of $Dy_2Ni_2L_{10}(bipy)_2$, **5**, obtained at 2 K and ±6 T is shown in Figure 9, and the magnetization obtained between 0 and 8 T is shown in the inset in Figure 10. The

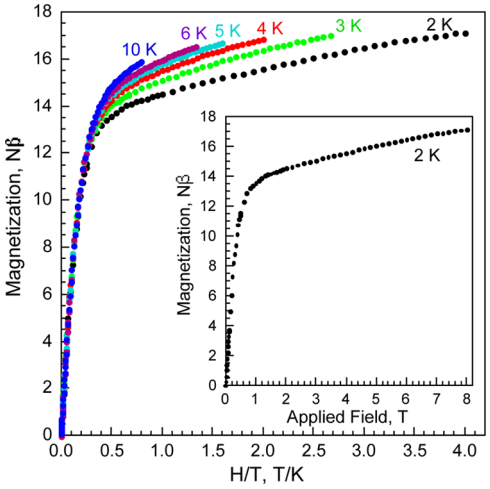

Figure 10. Isothermal magnetization of $Dy_2Ni_2L_{10}(bipy)_2$, **5**, as a function of H/T obtained between 0 and 8 T and between 2 and 10 K. Inset: The 2 K magnetization of **5**.

magnetization of **5** increases rapidly up to ca. 1 T, and at fields between 1 and 8 T increases more slowly to unsaturated values of 15.87(3) and 17.11(3) Nβ at 10 and 2 K, respectively. These clearly unsaturated values are significantly smaller than the M_{sat} = 24 Nβ as calculated (see above) on the basis of two dysprosium(III) ions with $g_{Dy(III)}$ = 4/3 and J_{max} = 15/2 and the spin-only contributions[20] of two nickel(II) cations with S = 1. *Ab initio* calculations, presented below, show that the magnetization could saturate at or slightly below 18 Nβ.

The variation in the nonsuperimposable isothermal magnetization of **5** with H/T (see Figure 10), in conjunction with both the rapid increase of the magnetization at low fields and its failure to saturate even at 8 T, indicates[16] the presence of either a significant magnetic anisotropy and/or low-lying excited states. Further, the ±15 Oe coercivity observed at 2 K for **5** is experimentally no different from zero. Hence **5** exhibits no hysteresis at 2 K, when the magnetization is measured with a sweep rate of a few mT/s, and strictly speaking cannot be considered to be a single-molecule magnet, but, as is shown below, ac magnetic studies do reveal slow relaxation of its magnetization even in the absence of any bias field.

The temperature dependence of the ac magnetization of **5** has been measured between 2 and 12 K in a ±3 Oe oscillating field, in the absence of a bias field, at several frequencies between 20 and 1500 Hz; the temperature and frequency dependence of χ_M' and χ_M'' for **5** is shown in Figure 11, and a Cole–Cole plot of χ_M'' vs χ_M' obtained for **5** between 2 and 6.5

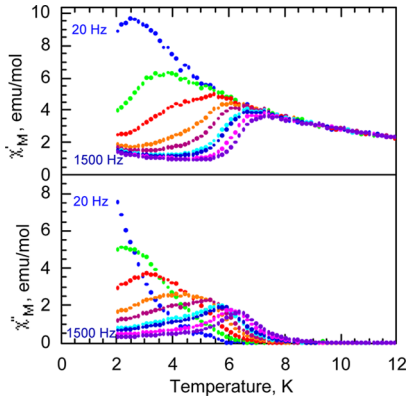

Figure 11. Temperature and frequency dependence of the in-phase, χ_M', and out-of-phase, χ_M'', components of the ac susceptibility of **5** obtained in the absence of any dc bias field. The increasing frequencies correspond to 20, 50, 100, 200, 300, 500, 600, 1000, and 1500 Hz.

K is shown in Figure 12. Again, in this figure the solid lines correspond to fits with the generalized Debye model[14] by using

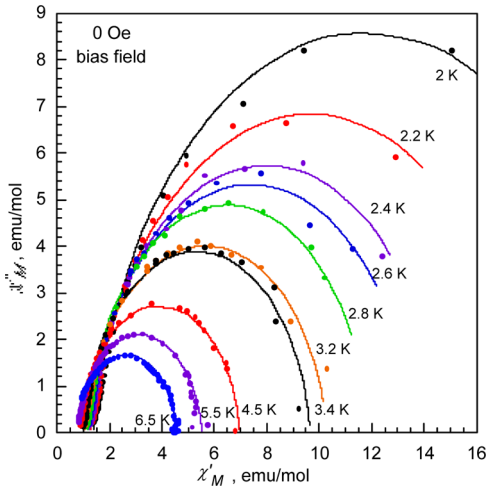

Figure 12. Cole–Cole plot for $Dy_2Ni_2L_{10}(bipy)_2$, **5**, obtained at selected temperatures between 2 and 6.5 K. The solid curved lines represent the best fit with the generalized Debye model.

the expressions given in the Supporting Information. In these fits, four parameters were fitted for each temperature, χ_∞, the adiabatic susceptibility extrapolated to infinite frequency, χ_0, the isothermal susceptibility extrapolated to zero frequency, τ, the magnetization relaxation time, and α, a parameter that quantifies the width of the τ distribution. For **5** all the α-values are ca. 0.2, values that are typical of this type of compound.

In a zero applied dc field, the AH^2T term in eq 1 vanishes and the fit for **5** (see Figure 13) yields a quantum tunneling frequency, τ_{QTM}^{-1}, of 120(14) s^{-1}, a Raman coefficient, C, of 0.44(4) s^{-1} K^{-5}, an attempt frequency constrained to a τ_0^{-1} of 54 × 10^9 s^{-1}, and an effective magnetization reversal barrier, U_{eff}, of 105(1) K or 73(1) cm^{-1}. In fitting the observed temperature dependence of the logarithm of τ, it was noted that the attempt frequency, τ_0^{-1}, was poorly defined and the frequency was kept constant to obtain the fit shown in Figure 13. Fits with τ_0^{-1} constrained between 54 × 10^9 and 10^{12} s^{-1} were statistically equivalent, and the effective magnetization barrier varied between 73(1) and 87(1) cm^{-1}. This range of

dx.doi.org/10.1021/ic501374q | Inorg. Chem. 2014, 53, 9785–9799

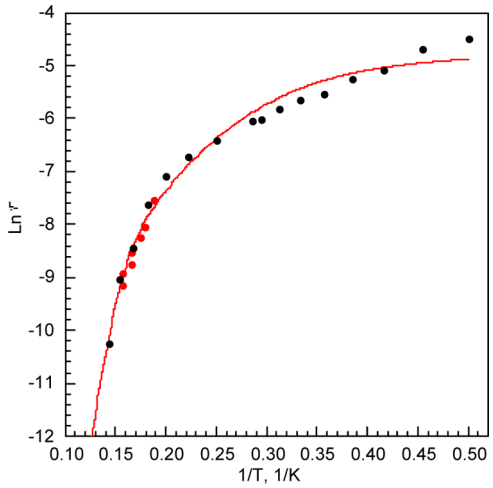

Figure 13. Arrhenius plot for $Dy_2Ni_2L_{10}(bipy)_2$, **5**. The red points have been obtained from the ac susceptibility measurements obtained between 50 and 1500 Hz shown in Figure 11. The black points have been obtained from the fit of the Cole−Cole plots shown in Figure 12. The red line is a least-squares fit, obtained with eq 1 and the parameters given in the text, of all the results obtained between 2 and 7 K.

attempt frequencies covers the values usually observed for various slow relaxing clusters and molecules.[15] The quantum tunneling frequency obtained for **5** is much smaller than that obtained for **1**, in agreement with the effect of the applied dc bias field on the magnetic relaxation of **1**. However, as is shown in Figure 13, no clear temperature-independent relaxation time is observed above 2 K, and, as a result, the 10% accuracy on the quantum tunneling frequency is somewhat poor.

The effective energy barrier for relaxation of the magnetization, U_{eff}, of 105(1) K or 73(1) cm^{-1} observed for **5** is among the largest U_{eff} values reported for other *Ln*−Ni-containing single-molecule magnet compounds[4,11b,d,21] for which the highest reported energy barrier is ca. 85 K or 59 cm^{-1}.[21] However, it should be noted that use of eq 1 to analyze the Arrhenius plot, rather than a linear fit as is often the case in many studies, is responsible for approximately one-half of this larger U_{eff} value. Indeed, if a linear fit of the Arrhenius plot between 5 and 7 K is used, a U_{eff} of 52(1) K or 35(1) cm^{-1} results.

Magnetic Properties of $Ho_2Ni_2L_{10}(bipy)_2$, 6. The temperature dependence of $\chi_M T$ for **6** obtained between 1.8 and 300 K in a 100 and 1000 Oe applied magnetic field is shown in blue in Figure 8. At 100 Oe the $\chi_M T$ of **6** decreases smoothly from 37.60(2) to 21.91(2) emu K/mol between 300 and 1.8 K; at 1000 Oe the decrease in $\chi_M T$ is from 35.00(2) to 22.86(2) emu K/mol between 300 and 1.8 K. The $\chi_M T$ is approximately linear above 150 K, but curvature in $1/\chi_M$ is clearly present in **6**, as is expected, at lower temperatures.

The value of $\chi_M T$ observed at 300 K and 100 Oe of 37.60(2) emu K/mol is substantially higher than the 30.13 emu K/mol expected for two holmium(III) ions and two nickel(II) ions if the latter each have $S = 1$ and $g = 2$. The higher value of $\chi_M T$ is a result of the presence of a large χ_0 (see Table 2) and also perhaps because the nickel(II) ions may have a small orbital contribution to their moments.

The continuous smooth decrease in $\chi_M T$ shown in blue in Figure 8 for **6** is quite different from the temperature dependence observed[4b] for $[L'_2HoNi_2][ClO_4]$. At this point it is difficult to understand the basis for these differences, differences that may be based on differing exchange coupling in the Ni···Ho···Ho···Ni bridging arrangement in **6** as compared to that of Ni···Ho···Ni in $[L'_2HoNi_2][ClO_4]$.

The magnetization of $Ho_2Ni_2L_{10}(bipy)_2$, **6**, obtained at 2 K and ±8 T is shown in Figure 9, and the results indicate that its magnetization at ±8 T is ±15.06(3) Nβ and not fully saturated. This value is substantially smaller than the 24 Nβ that would be expected (see the expression given above) for two holmium-

Table 3. *Ab Initio* Calculated Energies of Low-Lying Cation Spin−Orbit States in a Pseudo-octahedral Crystal-Field and Magnetic Properties for the Fragments

	fragment			
	$DyZnL_5(bipy)$	$LuCoL_5(bipy)$	$DyZnL_5(bipy)$	$LuNiL_5(bipy)$
complex	**1**	**1**	**5**	**5**
cation	Dy(III)	Co(II)	Dy(III)	Ni(II)
ground state	$^6H_{15/2}$	$^4F_{9/2}$ or $^4T_{1g}$	$^6H_{15/2}$	$^3F_4$ or $^3A_{2g}$
S	5/2	3/2	5/2	1
pseudospin, $\tilde{S}$	1/2	1/2	1/2	1
state	Kramers	Kramers	Kramers	non-Kramers
energy, cm^{-1}	0	0	0	0
	66.1(1)	101.5(1)	61.0(1)	6.3(1)
	124.4(1)	1644.1(1)	130.8(1)	10.1(1)
	166.8(1)	1758.4(1)	169.8(1)	7504.0(1)
	213.8(1)	2413.8(1)	221.9(1)	7625.2(1)
	252.8(1)	2471.5(1)	263.8(1)	7770.9(1)
	391.0(1)		407.4(1)	8610.9(1)
	451.8(1)		455.4(1)	8648.5(1)
g_x	0.041	5.80	0.031	2.30
g_y	0.083	4.04	0.052	2.27
g_z	19.36	1.94	19.41	2.23
μ_x, μ_B	0.020	2.90	0.015	2.30
μ_y, μ_B	0.041	2.02	0.026	2.27
μ_z, μ_B	9.68	0.97	9.71	2.23

dx.doi.org/10.1021/ic501374q | Inorg. Chem. 2014, 53, 9785−9799

(III) ions with $g_{Ho(III)} = 5/4$ and $J_{max} = 8$ and two nickel(II) ions with $g = 2$ and $S = 1$. No experimentally significant hysteresis is observed in the 2 K magnetization of **6**.

No frequency dependence of the in-phase, χ_M', or out-of-phase, χ_M'', components of the ac susceptibility of **6** was observed between 2 and 17 K and 20 to 9500 Hz; see Figure S10.

***Ab Initio* Calculations of the Magnetic Properties.** In order to obtain more insight into the magnetic properties of $Dy_2Co_2L_{10}(bipy)_2$, **1**, and $Dy_2Ni_2L_{10}(bipy)_2$, **5**, fragment *ab initio* calculations have been carried out by using the Molcas 7.8 program.[22]

The structures of the fragments used in the electronic and magnetic calculations are shown in Figure S11. The calculation of the electronic properties of a cobalt(II) or nickel(II) cation used a fragment in which the near-neighbor dysprosium(III) cation was replaced by its diamagnetic equivalent lutetium(III) cation. The calculation of the electronic properties of the dysprosium(III) cation used a fragment in which the near-neighbor cobalt(II) or nickel(II) cation was replaced by the diamagnetic equivalent zinc(II) cation. Thus, the cobalt(II) and nickel(II) calculations used the $LuCoL_5(bipy)$ fragment for **1** and the $LuNiL_5(bipy)$ fragment for **5**, and the dysprosium(III) calculations used the $DyZnL_5(bipy)$ fragment for both **1** and **5**. Details of the basis sets used in these calculations are given in Table S3. Because of the presence of an inversion center in **1** and **5**, only one dysprosium(III) and one cobalt(II) or nickel(II) fragment has to be used in the calculations. In these calculations the Cholesky decomposition threshold was set at 0.5×10^{-7} in order to save disk space.

A complete active space self-consistent field (CASSCF)[23] calculation has been carried out with seven 4f-type orbitals in the active space for dysprosium(III) and 10 3d and 3d′ orbitals in the active space for nickel(II) and cobalt(II). The 3d′-type orbitals have been included in order to test the double-shell effect,[24] which is considered to be important for a good description of excited states of transition metal cations. The second-order perturbation theory CASPT2 calculations were carried out only for the nickel(II) and cobalt(II) fragments with an imaginary shift of 0.1, where the imaginary shift in energy denominators is used to avoid intruder states. Further, all spin-free states of cobalt(II) and nickel(II) were mixed by spin−orbit coupling by using the SO-RASSI program.[25] In the case of the dysprosium(III) cation all 21 sextet states, 128 quartet states, and 130 doublet states were mixed because of disk space limitations. On the basis of the calculated energies of the spin−orbit states, the SINGLE-ANISO program[26] was used to compute the local magnetic properties of the fragments under study. The spin−orbit energies of the dysprosium(III), cobalt(II), and nickel(II) fragments are shown in Table 3. The accuracy of the calculated spin−orbit energies is $\pm 5 \times 10^{-8}$ hartree or ± 0.1 cm^{-1}.

The exchange coupling interactions between the magnetic metal cations were considered within the Lines model[27] as implemented with the POLY-ANISO program.[28] This model uses effective magnetic exchange coupling parameters with a Hamiltonian applied for the *ab initio* fragment wave functions. The magnetic properties of complexes **1** and **5** have been calculated in a fully *ab initio* approach, the only fitted parameter being the exchange coupling constant parameter J.

As we can see from Table 3, in both complexes **1** and **5** the dysprosium(III) cations are close to axial and the first excited Kramers doublets are placed at 66 cm^{-1} in **1** and at 61 cm^{-1} in **5** above the ground state. Therefore, the main difference in their magnetic properties is due to the presence of the cobalt(II) or nickel(II) cations. The zero-field splitting is much larger in the case of the cobalt(II) ion than in the case of the nickel(II) ion. To account for the exchange coupling, the following Lines Hamiltonian,[27]

$$\hat{H} = -2J_{Dy-M}\hat{\mathbf{S}}_{Dy}\cdot\hat{\mathbf{S}}_{M} - J_{Dy-Dy}\hat{\mathbf{S}}_{Dy}\cdot\hat{\mathbf{S}}_{Dy}$$

has been used, where M = Ni(II) or Co(II), and $\hat{\mathbf{S}}$ is the spin operator for the Dy(III), Co(II), and Ni(II), with $S_{Dy} = 5/2$, $S_{Co} = 3/2$, and $S_{Ni} = 1$.

The best fitting of the magnetic susceptibility data obtained at 1000 Oe is shown in Figure 14 and corresponds to the

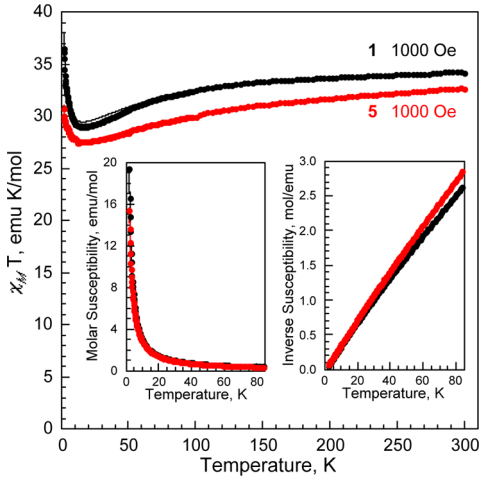

Figure 14. Temperature dependence of $\chi_M T$ of $Dy_2Co_2L_{10}(bipy)_2$, **1**, black, and $Dy_2Ni_2L_{10}(bipy)_2$, **5**, obtained in a 1000 Oe applied field, and the fit, solid lines, obtained between 2 and 85 K with the model described in the text. Left inset: The analogous χ_M results and fits. Right inset: The analogous $1/\chi_M$ results and fits. In the plots the solid line corresponding to the fit is almost completely hidden by the data points.

exchange parameters $J_{Dy-Co} = 0.2$ cm^{-1} and $J_{Dy-Dy} = 0.02$ cm^{-1} for **1** and $J_{Dy-Ni} = -0.2$ cm^{-1} and $J_{Dy-Dy} = 0.03$ cm^{-1} for **5**. The directions of the local magnetic moments in the ground exchange doublet of **1** and **5** are shown in Figure 15. The local magnetic moments of the dysprosium(III) cation from the ground exchange doublet are aligned along the main magnetic axis of dysprosium(III) in both **1** and **5**. In contrast, the local magnetic moments of the cobalt(II) and nickel(II) cations are not aligned along the dysprosium(III) axis because of the influence of the local anisotropy. The anisotropy of cobalt(II) is revealed directly by its g-tensor values, whereas the anisotropy of nickel(II) comes from the zero-field splitting, which is larger than the strength of the magnetic exchange interaction. In reality, the direction of the cobalt(II) and nickel(II) local moments is dictated by the interplay between the main magnetic and anisotropy axes, for cobalt(II) and nickel(II), respectively, and the exchange interaction of the transition metal cations with the dysprosium(III) cations.

To better understand the differences in the ac susceptibility behavior of $Dy_2Co_2L_{10}(bipy)_2$, **1**, and $Dy_2Ni_2L_{10}(bipy)_2$, **5**, the barriers for the reversal of their magnetizations have been constructed following a newly proposed methodology;[29] see Figure 16. The magnetic moment of the ground exchange doublet, arising in an applied magnetic field along the main

dx.doi.org/10.1021/ic501374q | Inorg. Chem. 2014, 53, 9785−9799

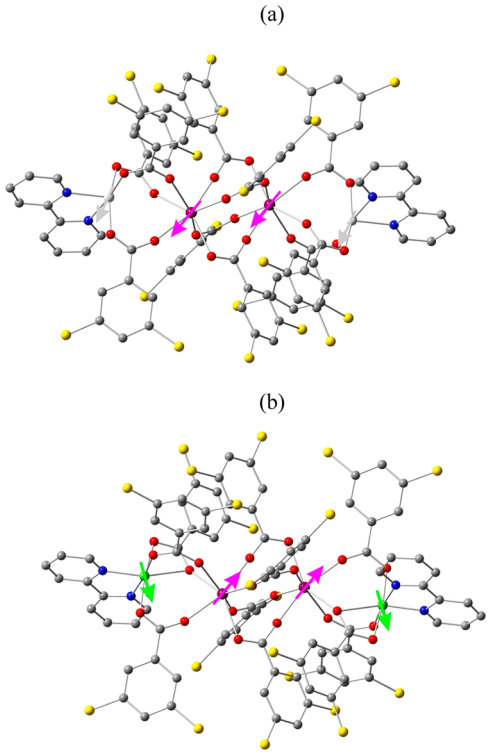

Figure 15. Calculated magnetic structure of **1** (a) and **5** (b). The arrows indicate the orientation of local magnetic moments in the ground exchange doublet state. Color scheme: Dy, purple; Co, light gray; Ni, green; O, red; Cl, yellow; N, blue; and C, gray. The hydrogen atoms have been omitted for clarity.

magnetic axis of this doublet, is obtained as a vector sum of induced noncollinear local magnetic moments of Dy(III) and M = Co(II) or Ni(II) (see Figure 15), $\boldsymbol{\mu} = 2(\boldsymbol{\mu}_{Dy} + \boldsymbol{\mu}_{M})$. The absolute value of the induced total moment is $|\boldsymbol{\mu}| = 3.95\ \mu_B$ for **1** and $|\boldsymbol{\mu}| = 5.6\ \mu_B$ for **5**.

It is apparent in Figure 16 that the reversal barrier for **1** is less than 1 cm^{-1}, whereas in **5** it is ca. 8 cm^{-1}. Therefore, the detection of this reversal barrier in **1** would require magnetic measurements below 1 K. In contrast, for **5**, in which the barrier is ca. 8 times larger, the reversal can be detected by measurements well above 1 K. Indeed, from Figure 13 it is apparent that at least two or more relaxation processes occur in **5**. One process at lower temperatures is associated with the reversal of exchange states, and a second process at higher temperatures is associated with relaxation through spin−orbit states of the individual dysprosium(III) cations.

The *ab initio* calculated first excited Kramers doublets of the individual dysprosium(III) cations are found at 66 and 61 cm^{-1} in **1** and **5**, respectively (see Table 3), values that are in good agreement with the experimentally determined reversal barriers of 82(2) and 73(1) cm^{-1}, respectively, in the absence of an applied field. A similar coexistence of distinct mechanisms for blocking the reversal of the magnetization has been reported in a $Dy^{III}_2Co^{II}_2$ complex.[18] If the exchange interactions were stronger in **1** and/or the measurements were carried out at temperatures below 1 K, then the coexistence of different relaxation mechanisms would be observed for **1** as well.

CONCLUSIONS

One new tetranuclear heterometallic cluster complex, $Dy_2Co_2L_{10}(bipy)_2$, **1**, and five new tetranuclear heterometallic

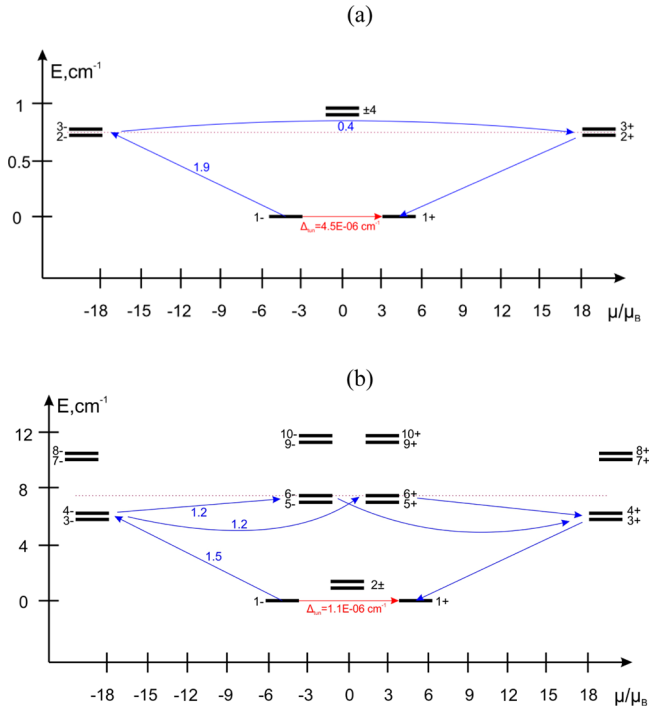

Figure 16. Low-lying exchange energy spectrum and the position of the magnetization reversal blocking barrier (dashed line) in $Dy_2Co_2L_{10}(bipy)_2$, **1** (a), and $Dy_2Ni_2L_{10}(bipy)_2$, **5** (b). The exchange states (short bold lines) are placed on the diagram according to their magnetic moments. The horizontal red arrows indicate the tunneling transitions within each doublet state, whereas the nonhorizontal curved blue arrows indicate the spin-phonon transition paths. The numbers at the paths are averaged transition moments in μ_B connecting the corresponding states. The blue arrows correspond to the maximal transition probability from a given state, therefore depicting the relaxation barrier for reversal of magnetization within the ground exchange doublet.

cluster complexes, $Ln_2Ni_2L_{10}(bipy)_2$, **2**−**6**, where *Ln* is a lanthanum(III), gadolinium(III), terbium(III), dysprosium(III), or holmium(III) cation, have been synthesized. In these complexes, the clusters have an approximately linear Co···Dy···Dy···Co or Ni···*Ln*···*Ln*···Ni cationic arrangement. All the complexes are paramagnetic above ca. 30 or 40 K.

The dc magnetic properties of the six complexes have been measured between 2 and 300 K. Whereas complexes **2**−**4** and **6** behave essentially as paramagnetic complexes between 2 and 300 K, complexes **1** and **5** exhibit more unusual magnetic properties. The presence of magnetic anisotropy in both **1** and **5** is evidenced by both the nonsuperimposability of the isothermal magnetization curves of **5** and their nonsaturated magnetization in an 8 T applied field. Further, the slow relaxation of the magnetization of **1** under a dc-applied field of 1000 Oe and of **5** under zero applied field is observed in the frequency and temperature dependence of their ac susceptibility. High effective energy barriers for the thermal activation of the reversal of the magnetization of 114.2(7) K or 79.4(5) cm^{-1} for **1** and 105(1) K or 73(1) cm^{-1} for **5** have been observed. These effective barriers are obtained from fits of the full Arrhenius plots of the logarithm of τ, the relaxation rate of the magnetization in **1** and **5**, with contributions from quantum tunneling, direct Raman scattering, and Orbach thermal processes.

dx.doi.org/10.1021/ic501374q | Inorg. Chem. 2014, 53, 9785−9799

The magnetic susceptibility of **1** and **5** has been calculated by *ab initio* methods, and the temperature dependence of their $\chi_M T$ product has been well fit with only two parameters: the exchange coupling parameters between the cobalt(II) or nickel(II) and the dysprosium(III) ions and between the two dysprosium(III) ions. The two reversal processes of the magnetization observed in **5** are analyzed through a new methodology. The calculated low-energy barrier of exchange type in **5** is calculated to be ca. 8 cm^{-1}, whereas it is smaller than 1 cm^{-1} and thus unobservable at temperatures above 1 K in **1**. The calculated high-energy barrier involves relaxation through excited Kramers doublets of the dysprosium(III) ions at 66 and 61 cm^{-1}, for **1** and **5**, respectively, in very good agreement with the measured energies of the magnetization reversal barriers.

Hence, we conclude that the slow magnetic relaxation of **1** and **5** results predominately because of the magnetic anisotropy of the dysprosium(III) cations, a conclusion that is in agreement with the observations reported[4,17,18] for other 3d transition metal cationic clusters containing dysprosium(III) cations. Further the difference in the relaxation mechanism of **1** and **5** results from the difference in the transition metal cations.

■ ASSOCIATED CONTENT

Ⓢ Supporting Information

The experimental section, X-ray crystallographic files in CIF format, tables of selected bond lengths and angles, and additional figures. This material is available free charge via the Internet at http://pubs.acs.org.

■ AUTHOR INFORMATION

Corresponding Authors

*E-mail: jmzheng@nankai.edu.cn.
*E-mail: Liviu.Chibotaru@chem.kuleuven.be.
*E-mail: glong@mst.edu.

Notes

The authors declare no competing financial interest.

■ ACKNOWLEDGMENTS

The authors thank J. M. Zadrozny and T. D. Harris for their help during the course of this work. This work was supported by the National Natural Science Foundation of China (50572040 and 50872057). V.V. and L.C. acknowledge the support of the Flemish Science Foundation (FWO) and of the University of Leuven through the INPAC and Methusalem programs.

■ REFERENCES

(1) (a) Leuenberger, M. N.; Loss, D. *Nature* **2001**, *410*, 789−793. (b) Wernsdorfer, W.; Aliaga-Alcalde, N.; Hendrickson, D. N.; Christou, G. *Nature* **2002**, *416*, 406−409. (c) Hill, S.; Edwards, R. S.; Aliaga-Alcalde, N.; Christou, G. *Science* **2003**, *302*, 1015−1018. (d) Lecren, L.; Wernsdorfer, W.; Li, Y. G.; Vindigni, A.; Miyasaka, H.; Clérac, R. *J. Am. Chem. Soc.* **2007**, *129*, 5045−5051. (e) Morimoto, M.; Miyasaka, H.; Yamashita, M.; Irie, M. *J. Am. Chem. Soc.* **2009**, *131*, 9823−9835. (f) Pedersen, K. S.; Bendix, J.; Clérac, R. *Chem. Commun.* **2014**, *50*, 4396−4415.

(2) (a) Costes, J. P.; Dahan, F.; Dupuis, A. *Inorg. Chem.* **2000**, *39*, 165−168. (b) Kido, T.; Ikuta, Y.; Sunatsuki, Y.; Ogawa, Y.; Matsumoto, N.; Re, N. *Inorg. Chem.* **2003**, *42*, 398−408. (c) Osa, S.; Kido, T.; Matsumoto, N.; Re, N.; Pochaba, A.; Mrozinski, J. *J. Am. Chem. Soc.* **2004**, *126*, 420−421. (d) Kajiwara, T.; Nakano, M.; Takaishi, S.; Yamashita, M. *Inorg. Chem.* **2008**, *47*, 8604−8606. (e) Kajiwara, T.; Takahashi, K.; Hiraizumi, T.; Takaishi, S.; Yamashita, M. *CrystEngComm* **2009**, *11*, 2110−2116. (f) Kajiwara, T.; Takahashi, K.; Hiraizumi, T.; Takaishi, S.; Yamashita, M. *Polyhedron* **2009**, *28*, 1860−1863. (g) Iasco, O.; Novitchi, G.; Jeanneau, E.; Wernsdorfer, W.; Luneau, D. *Inorg. Chem.* **2011**, *50*, 7373−7375. (h) Huang, X. C.; Zhou, C.; Wei, H. Y.; Wang, X. Y. *Inorg. Chem.* **2013**, *52*, 7314−7316. (i) Kühne, I. A.; Magnani, N.; Mereacre, V.; Wernsdorfer, W.; Anson, C. E.; Powell, A. K. *Chem. Commun.* **2014**, *50*, 1882−1885.

(3) (a) Chandrasekhar, V.; Pandian, B. M.; Azhakar, R.; Vittal, J. J.; Clérac, R. *Inorg. Chem.* **2007**, *46*, 5140−5142. (b) Chandrasekhar, V.; Pandian, B. M.; Vittal, J. J.; Clérac, R. *Inorg. Chem.* **2009**, *48*, 1148−1157. (c) Zou, L. F.; Zhao, L.; Guo, Y. N.; Yu, G. M.; Guo, Y.; Tang, J.; Li, Y. H. *Chem. Commun.* **2011**, 8659−8661. (d) Peng, J. B.; Zhang, Q. C.; Kong, X. J.; Zheng, Y. Z.; Ren, Y. P.; Long, L. S.; Huang, R. B.; Zheng, L. S.; Zheng, Z. P. *J. Am. Chem. Soc.* **2012**, *134*, 3314−3317. (e) Langley, S. K.; Ungur, L.; Chilton, N. F.; Moubaraki, B.; Chibotaru, L. F.; Murray, K. S. *Inorg. Chem.* **2014**, *53*, 4303−4315. (f) Chakraborty, A.; Bag, P.; Rivière, E.; Mallah, T.; Chandrasekhar, V. *Dalton Trans.* **2014**, *43*, 8921−8932. (g) Funes, A. V.; Carrella, L.; Rentschler, E.; Alborés, P. *Dalton Trans.* **2014**, *43*, 2361−2365.

(4) (a) Mori, F.; Ishida, T.; Nogami, T. *Polyhedron* **2005**, *24*, 2588−2592. (b) Chandrasekhar, V.; Pandian, B. M.; Boomishankar, R.; Steiner, A.; Vittal, J. J.; Houri, A.; Clérac, R. *Inorg. Chem.* **2008**, *47*, 4918−4929. (c) Colacio, E.; Ruiz-Sanchez, J.; White, F. J.; Brechin, E. K. *Inorg. Chem.* **2011**, *50*, 7268−7273. (d) Pasatoiu, T. D.; Sutter, J. P.; Madalan, A. M.; Fellah, F. Z. C.; Duhayon, C.; Andruh, M. *Inorg. Chem.* **2011**, *50*, 5890−5898. (e) Colacio, E.; Ruiz, J.; Mota, A. J.; Palacios, M. A.; Cremades, E.; Ruiz, E.; White, F. J.; Brechin, E. K. *Inorg. Chem.* **2012**, *51*, 5857−5868. (f) Cimpoesu, F.; Dahan, F.; Ladeira, S.; Ferbinteanu, M.; Costes, J. P. *Inorg. Chem.* **2012**, *51*, 11279−11293. (g) Chandrasekhar, V.; Bag, P.; Kroener, W.; Gieb, K.; Müller, P. *Inorg. Chem.* **2013**, *52*, 13078−13086.

(5) (a) Ferbinteanu, M.; Kajiwara, T.; Choi, K. Y.; Nojiri, H.; Nakamoto, A.; Kojima, N.; Cimpoesu, F.; Fujimura, Y.; Takaishi, S.; Yamashita, M. *J. Am. Chem. Soc.* **2006**, *128*, 9008−9009. (b) Abbas, G.; Lan, Y.; Mereacre, V.; Wernsdorfer, W.; Clérac, R.; Buth, G.; Sougrati, M. T.; Grandjean, F.; Long, G. J.; Anson, C. E.; Powell, A. K. *Inorg. Chem.* **2009**, *48*, 9345−9355. (c) Baniodeh, A.; Hewitt, I. J.; Mereacre, V.; Lan, Y.; Novitchi, G.; Anson, C. E.; Powell, A. K. *Dalton Trans.* **2011**, *40*, 4080−4086. (d) Abbas, G.; Lan, Y.; Mereacre, V.; Buth, G.; Sougrati, M. T.; Grandjean, F.; Long, G. J.; Anson, C. E.; Powell, A. K. *Inorg. Chem.* **2013**, *52*, 11767−11777.

(6) Rogez, G.; Rebilly, J. N.; Barra, A. L.; Sorace, L.; Blondin, G.; Kirchner, N.; Duran, M.; Slageren, J. V.; Parsons, S.; Ricard, L.; Marvilliers, A.; Mallah, T. *Angew. Chem., Int. Ed.* **2005**, *44*, 1876−1879.

(7) (a) Rinck, J.; Novitchi, G.; Heuvel, W. V.; Ungur, L.; Lan, Y.; Wernsdorfer, W.; Anson, C. E.; Chibotaru, L. F.; Powell, A. K. *Angew. Chem., Int. Ed.* **2010**, *49*, 7583−7587. (b) Sorace, L.; Benelli, C.; Gatteschi, D. *Chem. Soc. Rev.* **2011**, *40*, 3092−3104 and references therein.

(8) (a) Sessoli, R.; Tsai, H.-L.; Schake, A. R.; Wang, S.; Vincent, J. B.; Folting, K.; Gatteschi, D.; Christou, G.; Hendrickson, D. N. *J. Am. Chem. Soc.* **1993**, *115*, 1804−1816. (b) Sessoli, R.; Gatteschi, D.; Caneschi, A.; Novak, M. A. *Nature* **1993**, *365*, 141−143. (c) Mishra, A.; Wernsdorfer, W.; Abboud, K. A.; Christou, G. *J. Am. Chem. Soc.* **2004**, *126*, 15648−15649.

(9) (a) Andruh, M.; Costes, J. P.; Diaz, C.; Gao, S. *Inorg. Chem.* **2009**, *48*, 3342−3359. (b) Feng, X.; Zhou, W.; Li, Y.; Ke, H.; Tang, J.; Clérac, R.; Wang, Y.; Su, Z.; Wang, E. *Inorg. Chem.* **2012**, *51*, 2722−2724.

(10) Sheldrick, G. M. *SHELX-97, Suite of Programs for Solution and Refinement of Crystal Structures*; University of Göttingen: Göttingen, Germany, 1997.

(11) (a) Yamaguchi, T.; Sunatsuki, Y.; Kojima, M.; Akashi, H.; Tsuchimoto, M.; Re, N.; Osa, S.; Matsumoto, N. *Chem. Commun.* **2004**, 1048−1049. (b) Pasatoiu, T. D.; Etienne, M.; Madalan, A. M.; Andruh, M.; Sessoli, R. *Dalton Trans.* **2010**, *39*, 4802−4808. (c) Zheng, Y. Z.; Evangelisti, M.; Winpenny, R. E. P. *Angew. Chem., Int. Ed.* **2011**, *50*, 3692−3695. (d) Gao, Y.; Zhao, L.; Xu, X.; Xu, G. F.; Guo, Y. N.; Tang, J.; Liu, Z. *Inorg. Chem.* **2011**, *50*, 1304−1308.

(e) Meng, Z. S.; Guo, F. S.; Liu, J. L.; Leng, J. D.; Tong, M. L. *Dalton Trans.* **2012**, *41*, 2320−2329. (f) Yu, W. R.; Lee, G. H.; Yang, E. C. *Dalton Trans.* **2013**, *42*, 3941−3949.
(12) (a) Shannon, R. D.; Prewitt, C. T. *Acta Crystallogr.* **1969**, *B25*, 925−946. (b) Shannon, R. D.; Prewitt, C. T. *Acta Crystallogr.* **1970**, *B26*, 1046−1048. (c) Shannon, R. D. *Acta Crystallogr.* **1976**, *A32*, 751−767. (d) www.knowledgedoor.com/2/elements_handbook/shannon-prewitt_effective_ionic_radius.html. (e) Kahn, O. *Molecular Magnetism*; VCH Publishers, Weinheim, 1993. (f) Benelli, C.; Gatteschi, D. *Chem. Rev.* **2002**, *102*, 2369−2388.
(13) Towsif Abtab, S. M.; Chandra Majee, M.; Maity, M.; Titis, J.; Boca, R.; Chaudhury, M. *Inorg. Chem.* **2014**, *53*, 1295−1306.
(14) (a) Cole, K. S.; Cole, R. H. *J. Chem. Phys.* **1941**, *9*, 341−351. (b) Böttcher, C. J. F. *Theory of Electric Polarisation*; Elsevier: New York, 1952. (c) Aubin, S. M. J.; Sun, Z. M.; Pardi, L.; Krzystek, J.; Folting, K.; Brunel, L. C.; Rheingold, A. L.; Christou, G.; Hendrickson, D. N. *Inorg. Chem.* **1999**, *38*, 5329−5340. (d) Gatteschi, D.; Sessoli, R.; Villain, J. *Molecular Nanomagnets*; Oxford University Press: New York, 2006, and references therein.
(15) Zadrozny, J. M.; Atanasov, M.; Bryan, A. M.; Lin, C.-Y.; Rekken, B.; Power, P. P.; Neese, F.; Long, J. R. *Chem. Sci.* **2013**, *4*, 125−138.
(16) Lin, P. H.; Burchell, T. J.; Ungur, L.; Chibotaru, L. F.; Wernsdorfer, W.; Murugesu, M. *Angew. Chem., Int. Ed.* **2009**, *48*, 9489−9492.
(17) (a) Rinehart, J. D.; Long, J. R. *J. Am. Chem. Soc.* **2009**, *131*, 12558−12559. (b) Jiang, S. D.; Wang, B. W.; Su, G.; Wang, Z. M.; Gao, S. *Angew. Chem., Int. Ed.* **2010**, *49*, 7448−7451.
(18) Mondal, K. C.; Sundt, A.; Lan, Y.; Kostakis, G. E.; Waldmann, O.; Ungur, L.; Chibotaru, L. F.; Anson, C. E.; Powell, A. K. *Angew. Chem., Int. Ed.* **2012**, *51*, 7550−7554.
(19) Chilton, N. F.; Anderson, R. P.; Turner, L. D.; Soncini, A.; Murray, K. S. *J. Comput. Chem.* **2013**, *34*, 1164−1175.
(20) Bhunia, A.; Gamer, M. T.; Ungur, L.; Chibotaru, L. F.; Powell, A. K.; Lan, Y.; Roesky, P. W.; Menges, F.; Fiehn, C. *Inorg. Chem.* **2012**, *51*, 9589−9597.
(21) Chandrasekhar, V.; Bag, P.; Kroener, W.; Gieb, K.; Müller, P. *Inorg. Chem.* **2013**, *52*, 13078−13086.
(22) Aquilante, F.; De Vico, L.; Ferre, N.; Ghigo, G.; Malmqvist, P.-A.; Neograd y, P.; Pedersen, T. B.; Pitonak, M.; Reiher, M.; Roos, B. O.; Serrano-Andres, L.; Urban, M.; Veryazov, V.; Lindh, R. *J. Comput. Chem.* **2010**, *31*, 224−247.
(23) Roos, B. O.; Taylor, P. R.; Siegbahn, P. E. M. *Chem. Phys.* **1980**, *48*, 157−173.
(24) Andersson, K.; Roos, B. O. *Chem. Phys. Lett.* **1992**, *191*, 507−514.
(25) Malmqvist, P.-Å.; Roos, B. O.; Schimmelpfennig, B. *Chem. Phys. Lett.* **2002**, *357*, 230−240.
(26) (a) See the MOLCAS manual: http://molcas.org/documentation/manual/. (b) Chibotaru, L. F.; Ungur, L. *J. Chem. Phys.* **2012**, *137*, 064112.
(27) Lines, M. E. *J. Chem. Phys.* **1971**, *55*, 2977−2984.
(28) (a) Chibotaru, L. F.; Ungur, L.; Aronica, C.; Elmoll, H.; Pilet, G.; Luneau, D. *J. Am. Chem. Soc.* **2008**, *130*, 12445−12455. (b) Chibotaru, L. F.; Ungur, L.; Soncini, A. *Angew. Chem., Int. Ed.* **2008**, *47*, 4126−4129. (c) Chibotaru, L. F. Ab Initio Methodology for Pseudospin Hamiltonians of Anisotropic Magnetic Complexes. In *Advances in Chemical Physics*, 2nd ed., Vol. *153*; Rice, S. A.; Dinner, A. R., Eds.; Wiley: New York, 2013; pp 397−519.
(29) Ungur, L.; Thewissen, M.; Costes, J.-P.; Wernsdorfer, W.; Chibotaru, L. F. *Inorg. Chem.* **2013**, *52*, 6328−6337.